Scanning Tunneling Microscopy of Superconductors and High Field Electron Spin Resonance

vorgelegt von
Maximilian Uhl
aus Augsburg

Contents

Zusammenfassung (deutsch)

Diese Arbeit beschäftigt sich sowohl mit der Untersuchung von Supraleitern als auch Elektronenspinresonanz mittels eines Rastertunnelmikroskops. Die Kombination der atomaren Auflösung eines Rastertunnelmikroskops mit Elektronenspinresonanz erlaubt die Untersuchung der Spins einzelner Atome im Rahmen der Elektronenspinresonanzrastertunnelmikroskopie. Dazu werden einzelne Atome auf eine wenige Atome dicke isolierende Schicht aufgedampft. Ein externes Magnetfeld spaltet die Energiezustände der Elektronenspins dieser Atome aufgrund des Zeeman-Effekts auf. Wenn die Frequenz einer externen Mikrowelleneinstrahlung zur Zeeman-Aufspaltung korrespondiert, werden die Spinzustände angeregt. Unter Ausnutzung der Magnetoresistenz kann diese Anregung im Tunnelstrom zwischen dem aufgedampften Atom und einer spinpolarisierten Spitze gemessen werden. Um den g-Faktor des Spinsystems zu bestimmen wird entweder die Mikrowellenfrequenz oder das Magnetfeld variiert.

Die Rastertunnelmikroskopie einzelner Atome wird im Ultrahochvakuum und bei Temperaturen von weniger als 1 Kelvin durchgeführt. Bei der Elektronenspinresonanz werden sehr geringe Signale gemessen. Die thermische Anregung der Zustände ist dabei ein kritischer Faktor. Um das Verhältnis von Zeeman-Energie mit thermischer Energie zu verbessern, werden Elektronenspinresonanzrastertunnelmikroskopiemessungen bei Temperaturen von $300\,\mathrm{mK}$ und bisher unerreichten Frequenzen von $60\,\mathrm{GHz}$ bis zu $100\,\mathrm{GHz}$ demonstriert. Für die Einkopplung so hochfrequenter Signale über einen kontinuierlichen Frequenzbereich wurde eine spezielle Antenne ins Mikroskop eingebaut, die in einer Zusam-

menarbeit mit dem Karlsruhe Institute of Technolgy (KIT) entwickelt wurde.

Eine besondere Herausforderung stellt die Dämpfung des Hochfrequenzsignals auf dem Weg vom Signalgenerator bis zum Tunnelkontakt dar. Diese wird durch die Transferfunktion beschrieben und hängt stark nicht-linear von der Frequenz ab. Mit bekannter Transferfunktion kann die nicht-lineare Dämpfung kompensiert werden, um die Mikrowellenintensität während der Elektronenspinresonanzrastertunnelmikroskopiemessung konstant zu halten. Dafür muss die am Tunnelkontakt ankommende Strahlungsintensität in Abhängigkeit von der Frequenz gemessen werden. Da die Intensität am Tunnelkontakt nicht direkt zugänglich ist, kann sie nur indirekt gemessen werden. Dafür wurden verschiedene Messmethoden entwickelt und bestehende Methoden verbessert. Die entwickelten Methoden und Verbesserungen basieren auf der Tien-Gordon-Gleichung, die den Einfluss einer Mikrowellenstrahlung auf ein spannungsabhängiges Signal bescheibt.

Ein weiteres Quantenphänomen ist der Josephson-Effekt. Um diesen für den allgemeinen Fall mehrerer supraleitender Bänder zu analysieren, wurde der Typ-I-Zweibandsupraleiter Blei als Modellsystem untersucht. Der Tunnelstrom zwischen einer Pb(110)-Probe und einer Pb-Spitze in Abhängigkeit von Spannung und Normalzustandsleitfähigkeit enthält reichhaltige Informationen über die elektronische Struktur. Eine detaillierte theoretische Analyse der Messdaten erlaubt die Unterscheidug der Energielückenparameter der Spitze und der verschiedenen Probenbänder des Supraleiters. Die Berücksichtigung der Wechselwirkung mit der lokalen elektromagnetischen Umgebung und multiplen Andreev-Reflexionen erlaubt die Extraktion mikroskopischer Parameter: Die Verteilung des Stroms über mehrere Kanäle und mehrere Bänder kann charakterisiert werden. Ebenso können verschiedene Verbreiterungsmechanismen und Impedanzparameter der lokalen elektromagnetischen Umgebung bestimmt werden. Das entwickelte

4

Modell beschreibt die Messung mit hoher Präzision über mehrere Größenordnungen der Normalzustandsleitfähigkeit.

Abstract

This work is about the analysis of superconductors as well as electron spin resonance with a scanning tunneling microscope. The combination of the atomic resolution of a scanning tunneling microscope with electron spin resonance allows for the analysis of single atom spins by electron spin resonance scanning tunneling microscopy. For that, single atoms are evaporated on an insulating layer with a thickness of a few atoms. An external magnetic field splits the energy states of the electron spins of these atoms due to the Zeeman effect. If the frequency of an external microwave radiation corresponds to the Zeeman splitting, the spin states are excited. By making use of magnetoresistance, this excitation can be measured in the tunneling current between the evaporated atom and a spin polarized tip. In order to determine the g-factor of the spin system, either the microwave frequency or the magnetic field is varied.

Scanning tunneling microscopy of single atoms is done in ultra high vacuum and at temperatures of less than $1\,\mathrm{Kelvin}$. For electron spin resonance, very small signals are measured. The thermal excitation of states is a critical factor. In order to improve the relation between Zeeman energy and thermal energy, electron spin resonance scanning tunneling microscopy measurements are demonstrated at temperatures of $300\,\mathrm{mK}$ and so far unreached frequencies from $60\,\mathrm{GHz}$ up to $100\,\mathrm{GHz}$. For the irradiation of such high frequency signals over a continous frequency range, a special antenna that has been developed in a collaboration with the Karlsruhe Institute of Technology (KIT) was built into the microscope.

A special challenge is the attenuation of the high frequency signal on the way from the signal generator to the tunnel junction. It is described by the transfer function and depends strongly nonlinearly on frequency. With a known transfer function, the nonlinear attenuation can be compensated in order to hold the microwave intensity constant during the electron spin resonance scanning tunneling microspoce measurement. For that, the radiation intensity arriving at the tunnel junction must be measured in dependency of the frequency. As the intensity at the tunnel junction is not directly accessible, it can only be measured indirectly. Different measurement methods for that have been developed and existing methods have been improved. The developed methods and improvements are based on the Tien-Gordon equation that describes the influence of a microwave radiation on a signal that depends on voltage.

A further quantum phenomenon is the Josephson effect. In order to analyze it for the general case of multiple superconducting bands, the type I two-band superconductor lead is studied as a model system. The tunneling current between a Pb(110) sample and a Pb tip in dependency of voltage and normale state conductance includes rich information about the electronical structure. A detailed theoretical analysis of the measurement data allows to distinguish the superconductor's energy gap parameters of the tip and the different sample bands. The consideration of the interaction with the local electromagnetic environment and multiple Andreev reflections allows for the extraction of microscopic parameters: The distribution of current over multiple channels and multiple bands can be characterized. Furthermore, different broadening mechanisms and impedance parameters of the local electromagnetic environment can be determined. The developed model describes the measurement with high precision over multiple orders of magniude in normal state conductance.

1 Quantum Phenomena at the Nanoscale

Scanning Tunneling Microscopy is a powerful technique for the investigation of phenomena at the nanoscale. Since its development in 1981, its spatial resolution down to the single atom level stands out among all experimental methods, similarly met only by atomic force microscopy or scanning transmission electron microscopy. In a scanning tunneling microscope (STM), the tip, a sharply cut piece of wire, scans over a conducting surface line by line. A voltage between tip and sample produces a current that tunnels through the small empty space between tip and sample. Keeping the current constant in a feedback loop while varying the tip height delivers topographic information of the surface.

Using an STM allows not only for the analysis of purely spatial configurations like surface reconstructions, single molecules and impurities. By scanning tunneling spectroscopy (STS), electronic phenomena can also be analyzed with spatial resolution. In STS, the current in dependency of voltage is measured while the tip is typically stationary. This gives access to the electronic density of states due to the current's dependency on it. This yields information about a plethora of phenomena.

One phenomenon that may be studied is superconductivity. While it is known to exist already since 1911, its underlying mechanisms are only understood for simple cases. A full description of more complicated superconductor configurations is still needed. Superconductors conduct current with zero electric resistance. Additionally, if an external magnetic field is applied, a current emerges at the edge of the superconductor that creates a magnetic field

such that the total magnetic field becomes zero within the superconductor. A superconductor can only be in its superconducting phase below a critical temperature T_C and current density j_C, effectively also introducing a critical magnetic field B_C. Since this usually requires cooling by liquid helium, much effort has been put in the quest for a high-temperature superconductor. The discovery of cuprate and iron based superconductors increased T_C above liquid nitrogen temperature. However, those are unconventional superconductors which cannot be described in terms of the simplest theory, the BCS theory. In 2020, a hydrogen based superconductor at room temperature was found [72]. Hydrogen based superconductors require very high pressures, though. Therefore, insights about complicated superconductors are still needed.

Already before the invention of STM, superconductors' densities of states have been studied by preparing planar tunnel junctions. The use of STMs has added spatial resolution and precision. For example, this allowed for the study of a superconductor's order parameter in dependency of space [28] or of the influence of the electromagnetic environment [4].

Between two superconductors that are separated by an insulator, a supercurrent can appear. This is described by the Josephson effect. Josephson junctions are important for quantum technologies such as quantum computation. In the future, quantum technologies will require more complicated superconductor configurations including multiband superconductors. In this work, the multiband Josephson effect in the superconductor Pb is studied as a model system for multiband superconductivity.

A further important quantum phenomenon is magnetism. Electron spin resonance (ESR), also called electron paramagnetic resonance, investigates the magnetic moments of unpaired electrons. According to the Zeeman effect, the electrons' energy levels are split due to the application of a magnetic field depending on their g-factor. An electromagnetic wave with an energy that corresponds to the splitting can excite those states. By varying the

magnetic field or the electromagnetic wave frequency, the g-factor of the spin system can be found. This can be used for the identification of materials, for example. However, traditional ESR is a bulk technique meaning that it cannot access single atoms. By spin polarized STM, magnetic phenomena can be studied on the atomic level. However, true ESR-STM that can excite the single electron spins has only been realized since 2015 [7, 55, 58, 84, 88]. This technique also allows for the analysis of single spin interactions [5, 73, 82, 84]. The requirement of long averaging times due to high noise has always been a major challenge in ESR measurements. In this work, the temperature is reduced to 300 mK and the excitation frequency is increased to a so far unreached range from 60 to 100 GHz by an external antenna in order to realize ESR-STM outside of the thermal limit.

2 Theoretical Basics

2.1 Basics of Scanning Tunneling Microscopy

Amperemeter

Tip

Bias Voltage
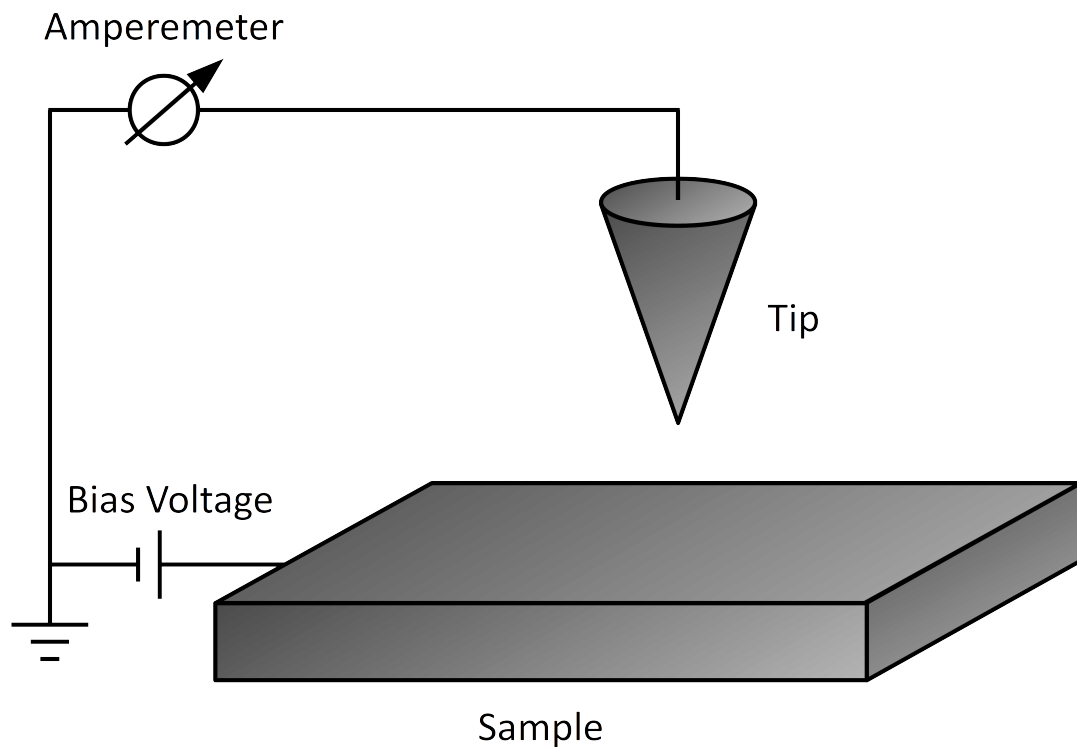
Sample

Figure 2.1: Schematic of a scanning tunneling microscope: A DC voltage is applied between tip and sample. The tunneling current between tip and sample is measured.

A scanning tunneling microscope (STM) can probe the atoms on the surface of an electrically conducting material. It was first developed by G. Binning, H. Rohrer, Ch. Gerber and E. Weibel [10]. The essential parts are a thin tip that probes an electrically conducting sample. The sample is typically of the size of a few

millimeters. The tip typically has a thickness of about half a millimeter. The position of the tip can be controlled on a pm scale in x-, y- and z-direction by applying high voltages to piezo crystals for the respective directions. Thereby, the tip scans over the surface line by line without touching it directly. A bias voltage is applied between tip and sample. Due to the tunneling effect, a tunneling current flows through the vacuum between tip and sample. This current is measured by an amperemeter (see Fig. 2.1). Measuring such small currents in the pA regime requires the use of a transimpedance amplifier. The current depends strongly on the distance between the sample and the last tip atoms. This strong dependence allows the measurement of small height differences of the surface.

In order to obtain atomic resolution, it is necessary to shield the STM against influences from the environment. Different levels of shielding are possible to improve accuracy. Dampers are used to reduce the effect of mechanical vibrations. The experiment is performed in ultra high vacuum to avoid surface contamination. By using a cryostat, the system can be cooled down to reduce atomic mobility and thermal excitations. Additionally, filters can be used to reduce electrical noise.

There are two possible measurement modes: In constant height mode, the tip height remains constant and the tunneling current is measured. In feedback mode, the height is varied to keep the current constant at a certain setpoint value. The height variation is controlled by a current feedback loop. This may introduce a delay in height adjustment which can be reduced by slower scanning. The feedback mode allows the measurement of the surface topography. This can make single atoms visible. Small height differences can be measured because the dependency of the current on height is strongly convex, namely approximately exponential. At the tip-sample distance z_0 where forces cancel each other out so that no net force is acting between tip and sample, the conductance G is equal to the quantum of conductance [10]

14

$$G_0 = \frac{2e^2}{h}. \tag{2.1}$$

According to the Landauer theory of the quantum of conductance and calculations of the work function ϕ, the dependence of the conductance G on the tip-sample distance z is [10]

$$G = G_0 \cdot \mathrm{e}^{-2\kappa(z-z_0)} \tag{2.2}$$

where $\kappa = \frac{\sqrt{2m\phi}}{\hbar}$. The work function ϕ of a metal surface describes the minimum energy that is needed to remove an electron from the bulk to the vacuum [10]. Equation (2.2) is only a very simple approximation, valid in the tunneling regime.

The tunneling current I depends on the density of states at the tip ρ_A and sample ρ_B, integrated over the applied bias voltage V. Additionally, the effect of thermal broadening can be described by a Fermi function f

$$f(E) = \frac{1}{1 + \exp\left(\frac{E - E_F}{k_B T}\right)}, \tag{2.3}$$

where T is the temperature, k_B the Boltzmann constant, E the energy and E_F the Fermi energy.

The total tunneling current is [10]

$$I = \frac{4\pi e}{\hbar} \int_{-\infty}^{\infty} \left(f\left(E_F - eV + \epsilon\right) - f\left(E_F + \epsilon\right)\right) \cdot$$
$$\cdot \rho_A\left(E_F - eV + \epsilon\right) \rho_B\left(E_F + \epsilon\right) |M|^2 \, \mathrm{d}\epsilon, \tag{2.4}$$

where e is the elementary charge, $\hbar$ Planck's constant, E_F the Fermi energy and $|M|$ the tunneling matrix element. The tunneling matrix element depends on the tip wavefunction χ and the sample wavefunction ψ as [10]

$$M = -\frac{\hbar^2}{2m} \int\limits_{\Sigma} \left(\chi^* \nabla \psi - \psi \nabla \chi^* \right) d\boldsymbol{S}. \qquad (2.5)$$

Here, Σ is a separation surface between tip and sample.

It is also possible to set the tip at a constant position above the sample and measure the current $I(V)$ in dependency of bias voltage. The $I(V)$ curve contains rich information about the densities of states. Calculating the derivative dI/dV of the current with respect to bias voltage allows to eliminate the integral over the bias voltage and thereby probe the densities of states of tip and sample. Typically, the dI/dV is not calculated from the $I(V)$ curve numerically, but measured separately by using a lock-in amplifier.

2.2 The Lock-in Technique

The lock-in technique is a general measurement method that allows for measuring small signal differences. It does so by applying an input signal at a certain frequency and decomposing an output signal with respect to that frequency. This effectively filters out noise at other frequencies. In the case of the $I(V)$ measurement in the STM, an AC voltage modulation ΔV is added to the DC bias voltage V. ΔV must be small so that $I(V)$ appears locally linear. The AC modulation frequency is typically chosen to be less than $1\,\text{kHz}$ to remain within the frequency resolution of the transimpedance amplifier. The resulting time-dependent current I is multiplied with a harmonic modulation of the same frequency. The phase difference between the input voltage modulation and the output current modulation is optimized such that the result is maximized. This yields a lock-in signal ΔI which is proportional to dI/dV. To obtain a $dI/dV(V)$ curve, this procedure is iterated over many points of bias voltage. To obtain a reasonable scale, the result can be normalized to the numerical derivative of the current. Analogously, the lock-in technique can also be applied to other cases as described later.

2.3 BCS Theory of Superconductors

BCS theory is the simplest theory that describes superconductivity microscopically rather than phenomenologically. It is named after Bardeen, Cooper and Schrieffer. According to BCS theory, superconducting charge carriers are pairs of two electrons, so called Cooper pairs. For the forming of a Cooper pair to become energetically favorable, a sufficient attractive interaction between the two electrons is required. This interaction can emerge due to mediation of positive ions in the atom lattice as well as the reduction of the Coulomb repulsion by the screening effect [76]. The role of the atom lattice points towards the importance of electron-phonon interaction. However, other mechanisms might be dominating for more exotic superconductors [76]. BCS theory can explain the experimental observation of an energy gap Δ proportional to $k_{\mathrm{B}}T_{\mathrm{C}}$ where k_{B} is the Boltzmann constant and T_{C} the critical temperature [76].

In terms of second quantization, the creation of an electron with momentum $\boldsymbol{k}$ and spin up is represented by the creation operator $c_{\boldsymbol{k}\uparrow}^{\dagger}$. Analogously, the destruction is described by the annihilation operator $c_{\boldsymbol{k}\uparrow}$. The BCS ground state is

$$|\psi_{\mathrm{G}}\rangle = \prod_{\boldsymbol{k}=\boldsymbol{k}_1,\ldots,\boldsymbol{k}_M} \left(u_{\boldsymbol{k}} + v_{\boldsymbol{k}} c_{\boldsymbol{k}\uparrow}^{\dagger} c_{-\boldsymbol{k}\downarrow}^{\dagger} \right) |\phi_0\rangle \qquad (2.6)$$

where $|\phi_0\rangle$ is the vacuum state, $|v_{\boldsymbol{k}}|^2$ the probability that the respective state is filled and $|u_{\boldsymbol{k}}|^2$ the probability that it is empty [76]. By assuming a pairing Hamiltonian

$$\mathcal{H} = \sum_{\boldsymbol{k}\sigma} \epsilon_{\boldsymbol{k}} n_{\boldsymbol{k}\sigma} + \sum_{\boldsymbol{k}l} V_{\boldsymbol{k}l} c_{\boldsymbol{k}\uparrow}^{\dagger} c_{-\boldsymbol{k}\downarrow}^{\dagger} c_{-l\downarrow} c_{l\uparrow} \qquad (2.7)$$

and defining the gap parameter as

$$\Delta_{\boldsymbol{k}} = -\sum_{l} V_{\boldsymbol{k}l} u_l v_l, \qquad (2.8)$$

a self-consistency condition for the gap parameter can be derived [76]:

$$\Delta_{\boldsymbol{k}} = -\frac{1}{2} \sum_l \frac{\Delta_l}{\sqrt{\Delta_l^2 + \xi_l^2}} V_{kl} \qquad (2.9)$$

where $\xi_l = \epsilon_l - \mu$ is the singe-particle energy relative to the Fermi energy. Finally, the Cooper pair forming probabilities can be calculated from this [76]:

$$v_{\boldsymbol{k}}^2 = \frac{1}{2}\left(1 - \frac{\xi_k}{\sqrt{\Delta^2 + \xi_k^2}}\right), \qquad (2.10)$$

$$u_{\boldsymbol{k}}^2 = 1 - v_{\boldsymbol{k}}^2. \qquad (2.11)$$

The density of states ρ_S in dependency of energy E of a superconductor is [76]:

$$\rho_\mathrm{S}(E) = \begin{cases} \rho(0) \cdot \frac{E}{\sqrt{E^2 - \Delta^2}}, & E > \Delta \\ 0, & E < \Delta \end{cases}. \qquad (2.12)$$

The density of states has a peak at the gap parameter Δ. ρ_S enters equation (2.4) for the tunneling current between superconductors.

2.4 The Josephson Effect

The Josephson effect describes the emergence of a supercurrent between two superconducting electrodes separated by an insulator. The insulator can also be the vacuum between the tip and the sample of an STM. The term supercurrent indicates that the charge carriers are Cooper pairs. The supercurrent I_S depends on the critical current I_C and the phase difference ϕ between the wave functions of the two superconducting electrodes as [26, 76]

$$I_\mathrm{S}(\phi) = I_\mathrm{C} \sin(\phi). \qquad (2.13)$$

The critical current is the current through the superconductor above which it can no longer remain superconducting. If no voltage is applied between the two electrodes, the phase difference

remains constant. Due to equation (2.13), different currents are possible at zero voltage. In order to measure the different possible currents from $-I_C$ to $+I_C$, it would be necessary to measure the voltage in dependency of a current bias. Usually the current is measured in dependency of a bias voltage instead in an STM.

If a voltage V is applied between the two electrodes, the phase difference is driven in time t [76]:

$$\frac{\mathrm{d}\phi}{\mathrm{d}t} = 2eV/\hbar. \tag{2.14}$$

The energy-phase relation $E(\phi)$ is a very fundamental property of a Josephson junction that may be different for different types of junctions. For all energy-phase relations, the total supercurrent is zero if the phase difference ϕ is zero [26]. For superconductors with time-reversal symmetry, the supercurrent is antisymmetric with respect to phase and therefore the supercurrent is zero if ϕ is an integer multiple of π [26]:

$$I_S(\pi n) = 0 \forall n \in \mathbb{Z}. \tag{2.15}$$

The critical current can be calculated from the energy-phase relation as follows:

$$I_C = \frac{2e}{\hbar} \max_\phi \left| \frac{\mathrm{d}E}{\mathrm{d}\phi} \right|. \tag{2.16}$$

In the case of low normal state conductance G_N, the critical current follows approximately the Ambegaokar-Baratoff formula [3]

$$I_C = \frac{\pi}{2e} G_N \Delta. \tag{2.17}$$

The gap parameter Δ can be generalized for unequal gap parameters Δ_t in the tip and Δ_s in the sample [3]:

$$\Delta = \frac{2}{\pi} \Delta_1 \cdot K \left(1 - \left(\frac{\Delta_1}{\Delta_2} \right)^2 \right) \tag{2.18}$$

where K is the complete elliptic integral of the first kind which describes the two unequal gap parameters. $\Delta_1 = \min(\Delta_t, \Delta_s)$ is

the smaller of the two gap parameters of tip and sample, $\Delta_2 = \max(\Delta_\mathrm{t}, \Delta_\mathrm{s})$ the larger of the two gap parameters. If $\Delta_\mathrm{t} = \Delta_\mathrm{s}$, the complete elliptic integral of the first kind is equal to $\frac{\pi}{2}$ and cancels out with $\frac{2}{\pi}$.

If a Josephson junction is formed between the tip and the sample of an STM, there are only few conduction channels due to the small size. These channels can have high transmission values. For high transmission and therefore high G_N, there can be deviations from the Ambegaokar-Baratoff formula (2.17). This can be explained by the non-sinusoidal energy-phase relation for Andreev bound states [71]

$$E(\phi) = \pm \Delta \sqrt{1 - \tau \sin^2\left(\frac{\phi}{2}\right)} \qquad (2.19)$$

where τ denotes the transmission. Its Fourier transformation is [71]:

$$E(\phi) = \sum_{m=-\infty}^{\infty} E_m \mathrm{e}^{im\phi} \qquad (2.20)$$

with the Fourier components

$$E_m = -\Delta \sum_{k=|m|}^{\infty} \begin{pmatrix} 1/2 \\ k \end{pmatrix} \begin{pmatrix} 2k \\ k+m \end{pmatrix} (-1)^{m+k} \left(\tau/4\right)^k . \qquad (2.21)$$

The index m represents the number of Cooper pairs being transferred. For low transmission, the coefficients E_m of higher order with respect to m decay quickly. By considering only the Fourier components up to first order $m = \pm 1$ in the energy-phase relation, the Ambegaokar-Baratoff formula (2.17) follows from equation (2.16).

If the temperature goes far below $1\,\mathrm{K}$, the system typically enters the dynamical Coulomb blockade regime where the phase is no longer well defined [71]. In ultrasmall junctions such as in an STM, the charging energy $E_\mathrm{C} = e^2/2C$ becomes larger than the thermal energy $k_\mathrm{B}T$ [38], especially if the STM is cooled to very

low temperatures. Here, e is the elementary charge and C the junction capacitance. In this case, the interaction of the tunneling electron with the local electromagnetic environment has to be considered. $P(E)$ theory [38] describes the probability P at which the tunneling electron exchanges an energy E with the environment.

With $P(E)$ theory [16, 39], the Josephson current in dependency of voltage can be described in terms of the local electromagnetic environment,

$$I(V) = \frac{\pi e E_\mathrm{J}^2}{\hbar} \left(P(2eV) - P(-2eV) \right), \qquad (2.22)$$

where E_J is the Josephson energy. E_J determines the critical current I_C. The environment enters the calculation as an electromagnetic impedance described by a capacitance C_J and a transmission line model. The impedance of the transmission line without C_J is described by [4]

$$Z(\omega) = R_\mathrm{DC} \cdot \frac{1 + \frac{i}{\alpha} \tan\left(\frac{\pi}{2} \frac{\omega}{\omega_0} \right)}{1 + i\alpha \tan\left(\frac{\pi}{2} \frac{\omega}{\omega_0} \right)}. \qquad (2.23)$$

This transmission line has the following three parameters: The environmental DC resistance R_DC, the effective damping parameter α and the frequency of the principal resonance ω_0 [4]. Together with the capacitance C_J, the total impedance $Z_\mathrm{t}(\omega)$ becomes [4]

$$Z_\mathrm{t}(\omega) = \frac{1}{i\omega C_\mathrm{J} + Z^{-1}(\omega)}. \qquad (2.24)$$

The function $P(E)$ that describes the inelastic tunneling can be calculated from the total impedance $Z_\mathrm{t}(\omega)$ [4] as the energy exchange with the environment depends on its impedance.

2.5 Electron Spin Resonance

Electron spin resonance scanning tunneling microscopy (ESR-STM) combines the established techniques of electron spin resonance,

also called electron paramagnetic resonance, with the atomic resolution of an STM to measure the spins of single atoms [7, 55, 58, 84, 88]. It has first been demonstrated with Fe atoms on an MgO film [7].

Spin resonance measures the excitation of spin states of electrons or atomic nuclei. Cooling the system down ensures a spin state initialization in the ground state. To lift the spin state degeneracy, a magnetic field has to be applied. The magnetic field may be applied externally or come from the local environment. If an external radiation is applied, the spin state will be driven out of its ground state only if the radiation frequency corresponds to the energy difference between the spin states.

One way of doing the measurement in the STM is to pick up an atom to the tip to make it spin-polarized and then move the tip above another spin system. If the external radiation excites the spin state, this will change the magnetoresistance between tip and sample atom depending on the relative orientation of sample atom spin and tip atom spin. Therefore, the excitation can be measured in the tunneling current.

The difference in tunneling current is small, though. To measure it nonetheless, a lock-in technique can be applied [57]. Here, the external radiation is repeatedly switched on and off with a much smaller switching frequency than the radiation frequency. The tunneling current is then demodulated with respect to the switching frequency. Thereby, a lock-in signal is obtained that shows a clear difference in magnetoresistance only at radiation frequencies that correspond to the magnetic field [7]. The signal can also be measured in dependency of time to observe Rabi oscillations between the spin states [88]. This requires phase coherence of the spin states.

3 Experimental Setup

3.1 General Setup

We use the commercial STM system Unisoku USM1300 which was modified to fit high frequency cabling from outside through the vacuum space to the STM. In order to decouple the STM from mechanical vibrations, it is installed on a concrete block that is carried by an active isolation air daming system from Bilz Vibration Technology AG that consists of four air dampers, one on each corner of the concrete block. The air dampers are all actively controlled by a controller that regulates the pressure in the air tubes to each damper. Additionally, on top of the block, there is a damping table that carries the cryostat and the vacuum chamber. As a third decoupling stage, the STM itself is hung up on springs inside the cryostat.

The vacuum chamber is mounted directly on top of the damping table. It consists of an exchange chamber (EXC) and a load-lock chamber (LLC) which are connected to each other through a valve (see Fig. 3.1). Tips and samples are transferred from the outside into the load lock chamber and from there to the exchange chamber. An ion pump with a Ti sublimation pump (TSP) is attached to the exchange chamber. There is one turbo pump attached to the exchange chamber (EXC-TMP) and another one at the load-lock chamber (LLC-TMP). Both turbo pumps are connected to the same rough pump through valves. The first thing to do to bring the chamber from ambient pressure to ultra high vacuum is to activate only the rough pump to pump out most of the air. After approximately half an hour, the turbo pumps are activated. Then, the chamber is baked with heating tapes for a week at tem-
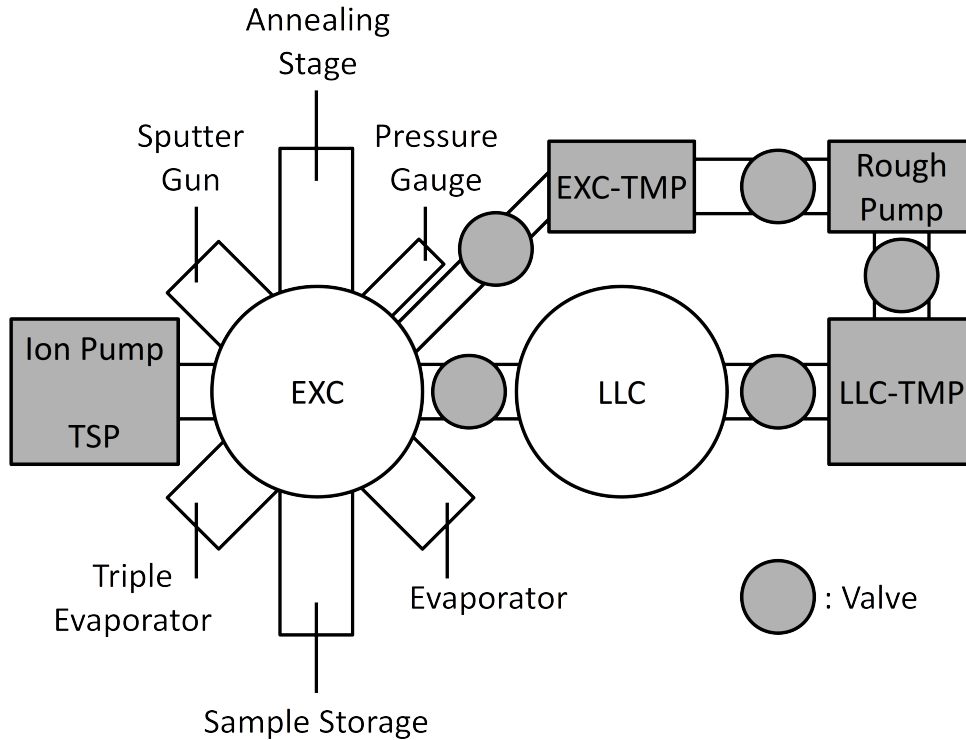
Figure 3.1: Top view of the vacuum chamber: Tips and samples are transferred through the load lock chamber (LLC). Connected with it through a valve, there is the exchange chamber (EXC) which is used for tip and sample preparation. Each chamber has their respective turbo pump (TMP). Additionally, there is an ion pump and a Ti sublimation pump (TSP).

peratures of a bit less than $150\,°C$ so that remaining moisture is evaporated and pumped out. After that, a pressure of around 10^{-7} to $10^{-8}\,$mbar can be achieved. By activating the ion pump, the pressure can be lowered further. The Ti sublimation pump removes further remaining reactive molecules such as hydrogen. In contrast to the other pumps, it does not run continuously, but only for some seconds a day. With this procedure, a minimum pressure of $2 \cdot 10^{-10}\,$mbar is achieved. During the STM measurement, the turbo pumps and the rough pump are turned off in order to minimize mechanical vibrations. The ion pump can keep the vacuum up in the chamber during that time.

Sample preparation is done in the exchange chamber to which a sputter gun and an annealing stage are attached. Evaporators can also be attached to the exchange chamber. The cryostat which contains the STM is located under the vacuum chamber within a pit in the concrete block. Tip, sample and radiation shields can be transferred from the exchange chamber to the STM through a valve located below the exchange chamber. This is done by the use of a vertical transfer rod that is fitted in a tube above the rest of the exchange chamber. It can grab the items to be transferred by a bayonet cap. The tip is located under the sample. Above the sample, up to two radiation shields can be installed which are required to cool the STM to the minimum temperature.

In order to avoid ground loops and to reduce electrical noise, the measurement devices are not directly connected to the measurement computer that controls them. Instead, the measurement devices are connected to a switch over ethernet. This switch is connected to the computer via fiber optics cables. This requires the installation of a fibre optics card in the measurement computer's mainboard. The measurement devices and the fibre optics switch are electrically powered through a galvanic isolation to decouple them from the noise of the measurement power network.

3.2 Cryostat

We use a Cryogenic cryostat with a superconduting magnet. Initially, the cryostat is precooled by liquid nitrogen down to its evaporation temperature of $77\,\mathrm{K}$. From then on, only liquid helium is used for the regular operation. Liquid helium has an evaporation temperature of $4.2\,\mathrm{K}$ at ambient pressure. The cryostat has to be refilled twice per week with about $60\,\mathrm{litres}$ of liquid helium for each refill. Inside the cryostat, there is an ultra high vacuum (UHV) volume where the STM is located (see Fig. 3.2). It is isolated from the liquid helium volume by an intermediate vacuum chamber (IVC). The IVC is regularly pumped by a turbo pump to
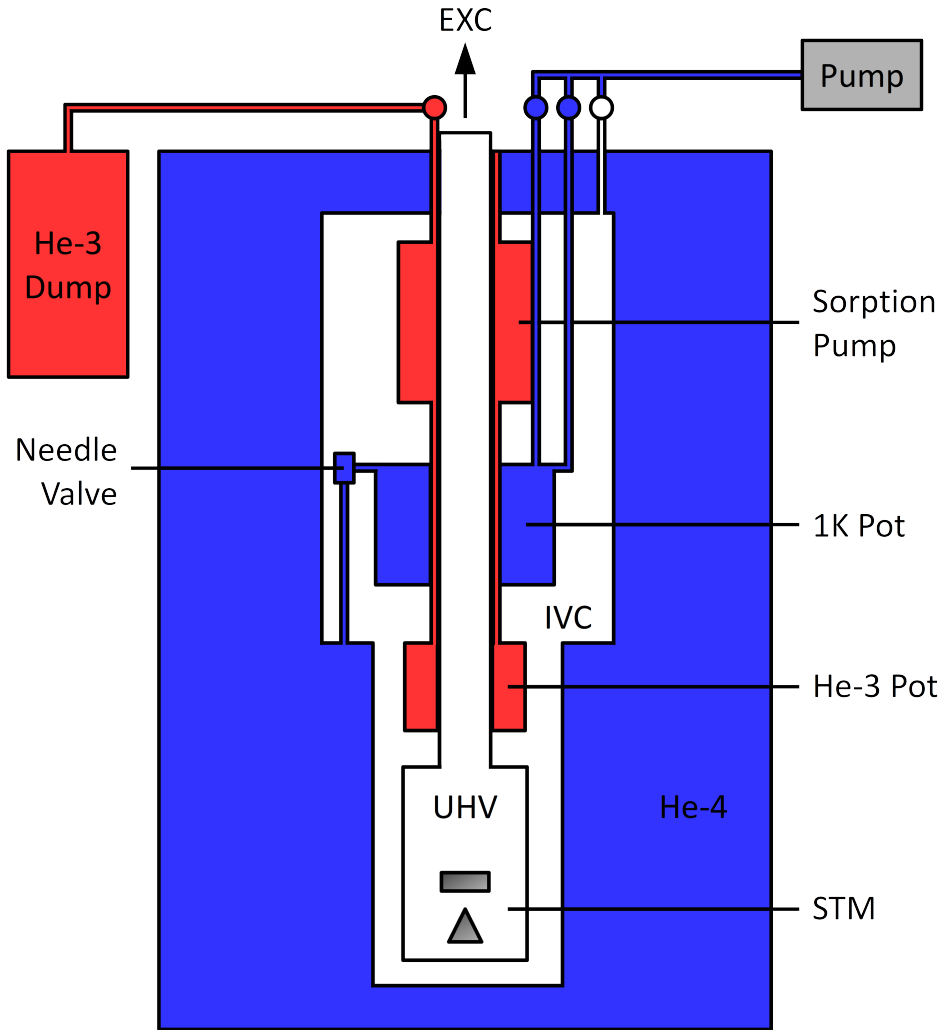
Figure 3.2: Schematic of the cryostat in side view: Volume with He-4 is depicted in blue, He-3 in red and vacuum in white. The three valves that are connected to the pump can be used to either pump the intermediate vacuum chamber (IVC), the 1K pot line or the He-4 line that cools the sorption pump. The ultra high vacuum space (UHV) is connected to the exchange chamber (EXC) through a valve.

achieve good thermal and mechanical isolation from the cryostat. The pumping of the IVC is important because residual water may freeze inside the IVC and form an undesired mechanical bridge. Liquid helium is pumped through a tube through a 1K pot which is weakly thermally coupled to the STM. The evaporation temperature of helium increases with pressure. Pumping on the 1K pot

reduces the pressure. Therefore, the evaporation temperature of the helium is reduced by pumping on it. As the temperature of the 1K pot adapts to the evaporation temperature of the helium, pumping on the 1K pot reduces its temperature. The opening to the 1K pot is controlled by a needle valve. By carefully tuning the needle valve, a typical minimum 1K pot temperature of 1.6 K is reached.

The use of the isotope helium-3 allows even further cooldown: Helium-3 has a phase diagram that is different from helium-4. It has even lower evaporation temperatures at low pressure. This allows a cooldown to 300 mK. Up to 30 l of helium-3 gas is used. It is kept in three volumes that are connected to each other: A helium-3 volume inside the UHV space that is strongly thermally coupled to the STM, a sorption pump and an external dump outside of the cryostat. The dump is connected to the other volumes through a valve and is mainly a safety space for the helium in the case of unexpected overpressure. By cooling the sorption pump, the helium-3 gas will be sucked into the sorption pump. By heating it, it will push the helium-3 out. In order to operate the STM at 300 mK, it is necessary to condense the helium-3 in the helium-3 space at the STM. For that, the needle valve is adjusted such that the 1K pot and the sorption pump reach minimum temperature. The helium-3 is thereby sucked into the sorption pump. Then, the sorption pump is slowly heated up to 50 K such that the helium-3 gas condenses at the cold 1K pot. If the heat-up is done too fast, the 1K pot cooling is insufficient so that not all of the helium-3 is condensed. After the condensation procedure, the helium-3 evaporates slowly. The holding time is approximately 70 hours. Heating the system, for example by activating our built-in microwave, can reduce the holding time drastically, depending on the power.

The magnetic field goes up to 6 T at a current of 77.85 A. After the magnet has been energized up to a certain current, it can be operated in persistent mode. This allows the disconnection

of the magnet power supply to reduce electrical noise during the
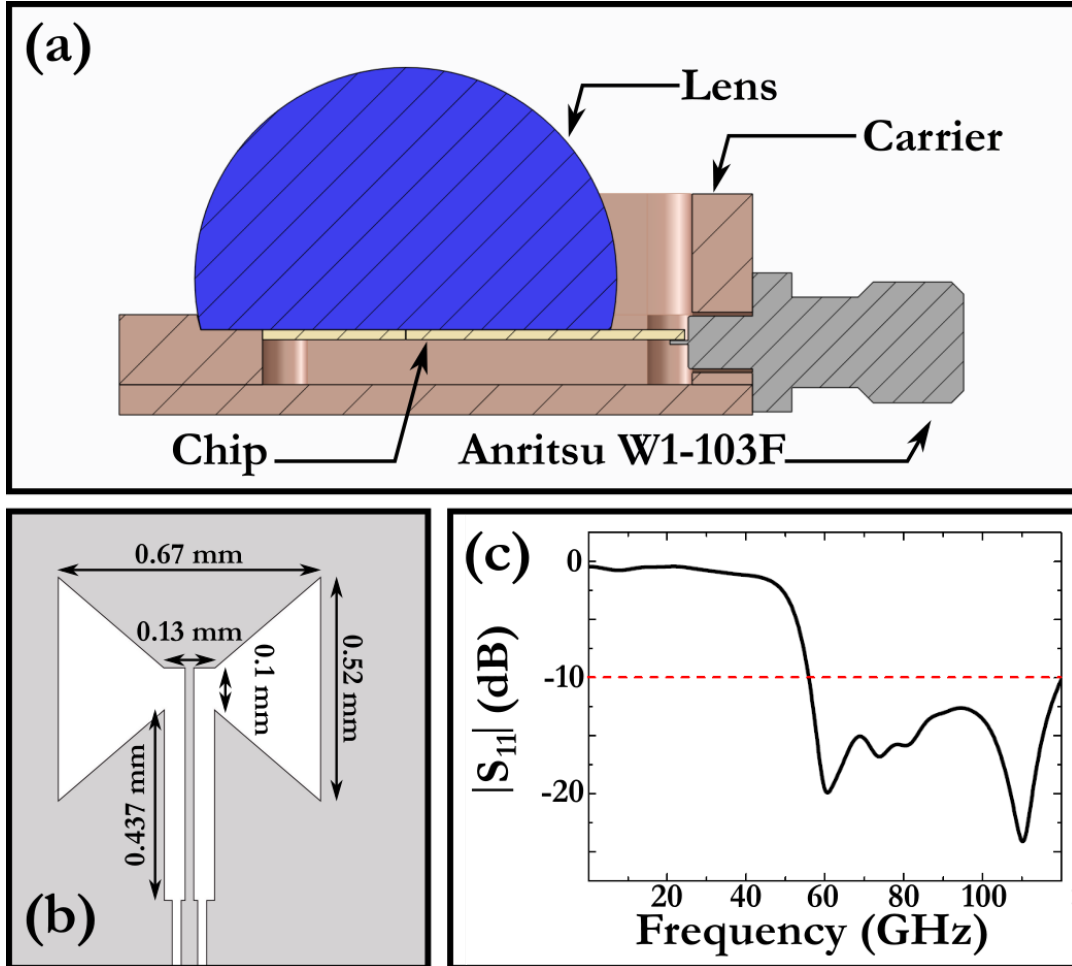measurement.

3.3 Microwave Antenna

Figure 3.3: This figure about the design of our antenna is taken from our pa-
per [18]. (a) The antenna carrier with a hyperhemispheric Si lens
(b) The antenna geometry: The AuPd is shown in grey. (c) The
simulated reflectance characteristics of the antenna in dependency of
frequency: It shows that the antenna works well from 60 to 120 GHz.
Figures (b) and (c) are originally from the work of J. Merkt [52]

The microwave antenna has been developed in a collaboration
with the Karlsruhe Institute of Technology (KIT) as the Bachelor

thesis of Jonas Merkt [52]. In order to cover a broad frequency range, a broadband bowtie antenna geometry is used. It has been designed by using CST Microwave Studio software with performance tests in 8.4:1 scale models. The antenna is cut out of a AuPd film on an Si substrate as shown in Fig. 3.3 (b). The antenna itself would radiate a bit in all directions. In order to focus the radiation mainly towards the STM tunnel junction, an Si hyperhemispheric lens is used on top of the antenna (see Fig. 3.3 (a)). The simulated frequency dependent antenna characteristic is shown in Fig. 3.3 (c).
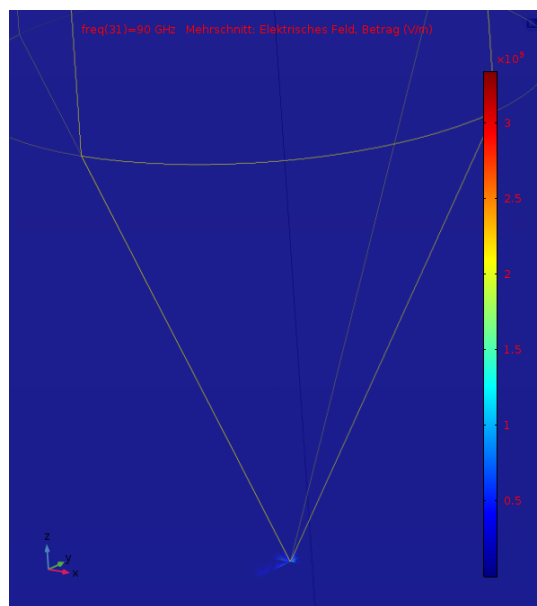

Figure 3.4: Simulation of the STM tip apex with Comsol Multiphysics: The electric field is strongly focussed at the tip apex and much smaller at the rest of the tip

Using the Comsol Multiphysics software, further simulations of the antenna have been performed to consider the local geometry at the tunel junction. This simulation uses the finite elements method (FEM) and the constant frequency formulation of Maxwell's equations for different frequencies, respectively. This simulation shows that the electric field is strongly enhanced at the apex of the tip (see Fig. 3.4). The magnitude of the field enhancement depends on the field polarization and frequency.
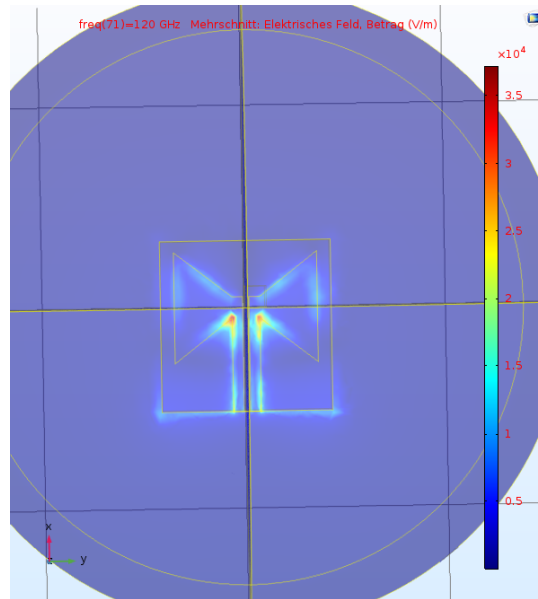
Figure 3.5: Simulation of the antenna with Comsol Multiphysics: The distribution of the electric field over the two bowties compared to inner and outer conductor is shown.
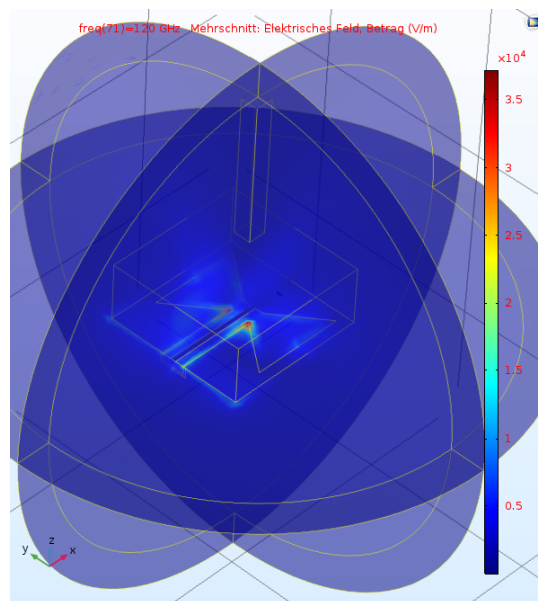

Figure 3.6: Simulation of the antenna with Comsol Multiphysics: Si cuboids of different thickness on top of the antenna chip are simulated to approximate and understand the effect of the hyperhemispheric Si lens. The Si layer focuses the radiation towards the direction of the Si.

In order to understand the effect of the Si lens, simulations with different Si substrate thicknesses were carried out. They show that thicker Si substrates amplify the electric field at the bowtie part compared to the lower part where inner and outer conductor are parallel (see Fig. 3.5). Also, the field is enhanced towards the side with the Si substrate (see Fig. 3.6).

3.4 Measurement Program

A powerful measurement program has been developed in LabView. It is based on the Nanonis Programming Interface for the Nanonis Scanning Probe Microscopy (SPM) Software from SPECS. Furthermore, it uses the Keysight LabView interface to communicate with the Keysight frequency generator and virtual instrument software architecture (VISA) commands to communicate with the Cryogenic magnet controller. Measurements without microwave or without magnetic field are also possible and the program can also be used if frequency generator or magnet are disconnected, respectively. The graphical user interface (GUI) is shown in Fig. 3.7.

The program is capable of performing all STM measurements presented in this thesis. Its basic functionality is to measure the current and arbitrary further parameters in up to four-dimensional maps with the following four dimensions: Bias voltage, microwave frequency, microwave attenuation and magnetic field. Measuring one-dimensional ESR frequency sweeps or ESR magnetic field sweeps are therefore only some of the most basic features of the program.

Measurements with high resolution or dimensionality can take many hours. Automating these allows for more efficient measurements that can also be done over night. Before every measurement, the program calculates how long the measurement will take, making the lab work easier to schedule.

With a known transfer function that translates the microwave input power to the voltage amplitude that arrives at the tunnel
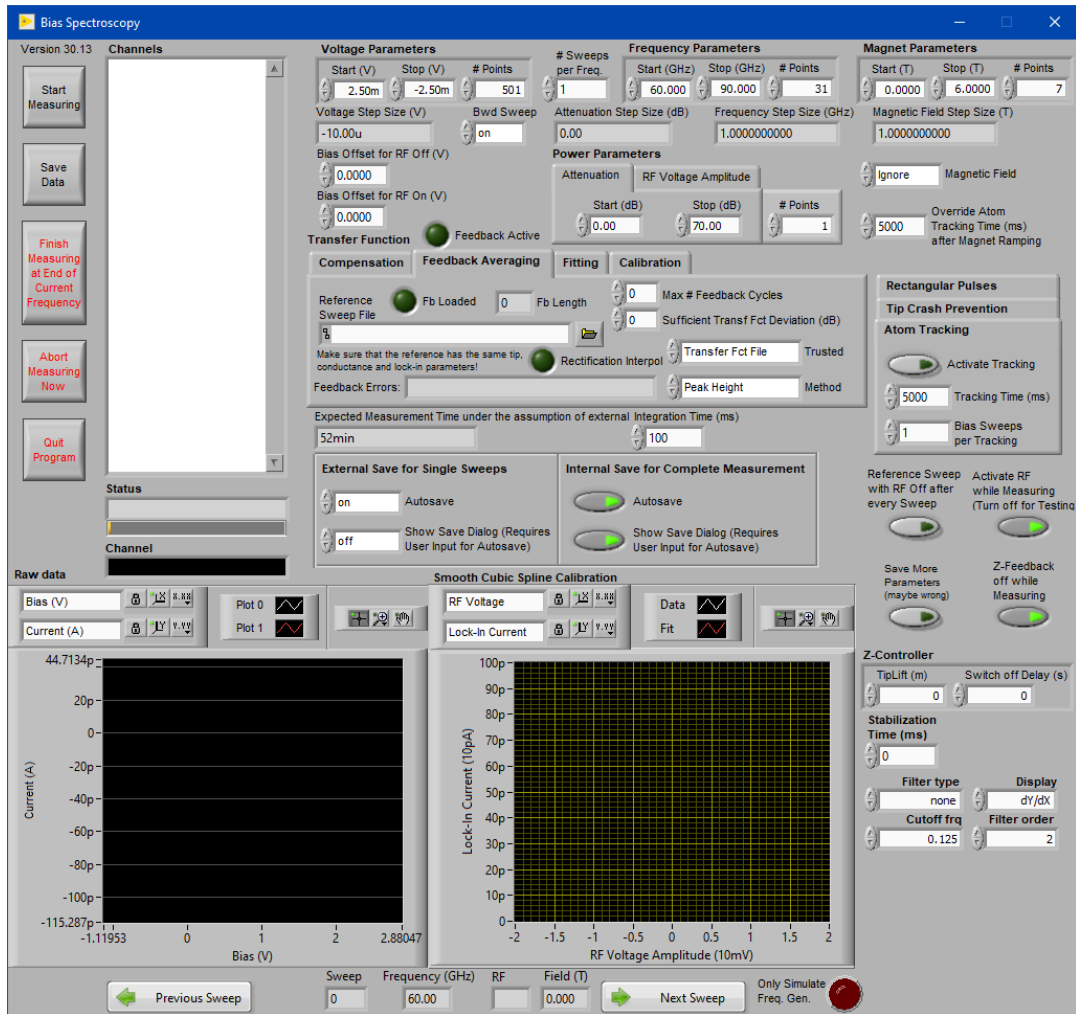
Figure 3.7: Bias Spectroscopy Program Version 30.13 GUI: The four parameter clusters for voltage, frequency, power and magnet are apparent. In the white space on the top left, all channels from the Nanonis SPM Software are loaded on program start. The graph on the bottom left shows the last bias voltage sweep and the graph on the bottom right shows the calibration curve for the transfer function (see section 4.5). There is one tab for transfer function compensation and three for transfer function measurement, namely feedback averaging, fitting and calibration. On the right, there are settings for extra features like atom tracking and tip crash prevention.

junction, the program can also iterate through the microwave's arriving voltage amplitude instead of input power. The transfer function can be imported as a formatted text file into the program.
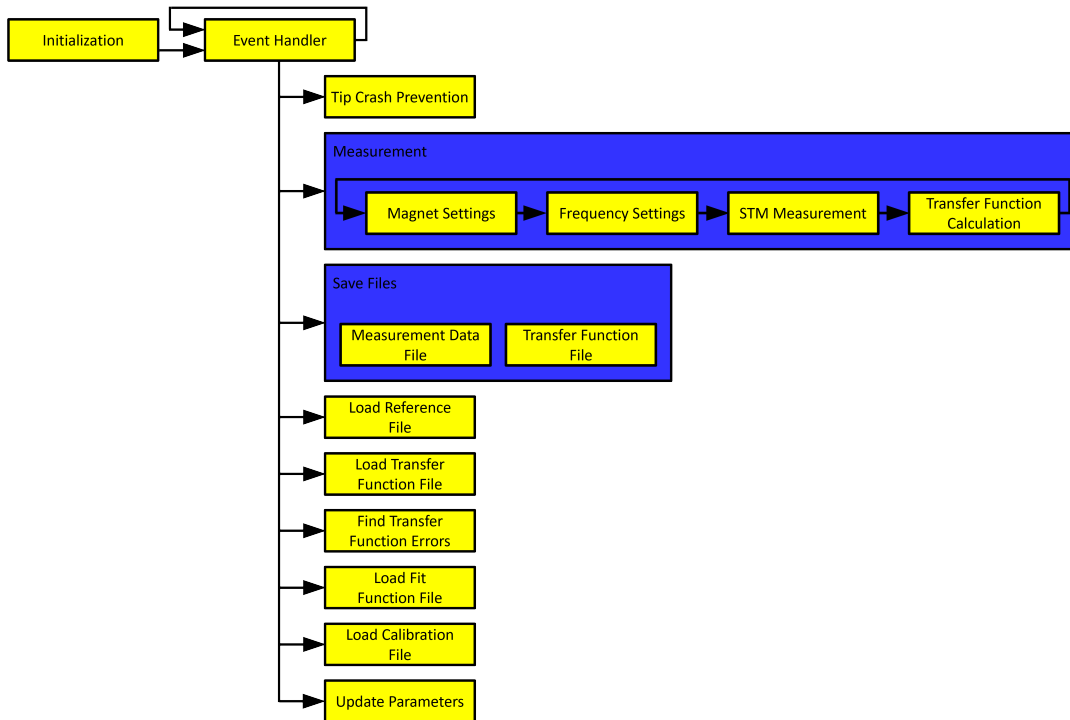
Figure 3.8: Bias Spectroscopy Program Scheme: Only the most important events are shown in this simplified schematic. There are many more events in the actual program.

The program also implements all transfer function measurement methods including their respectve fitting routines that are described in this thesis. It also allows for importing custom fit functions. After a transfer function measurement, it outputs a transfer function file that can be imported directly in the program.

Some analysis procedures require a reference sweep without microwave in order to fit a sweep with microwave. Therefore, alternating sweeps with microwave on and off are also implemented. If a single reference sweep is enough to fit multiple microwave sweeps, the single reference sweep can be imported into the program. However, repeating the reference sweep after every microwave sweep is safer because the tip may change during a long measurement which may change the reference sweep.

Microwave chopping is also possible: Here, the microwave alternates between equal times of being on and off with an arbitrary

frequency. Typically, a chopping frequency of 80 Hz is used. This allows for locking into the signal difference between microwave on and off which is important for transfer function measurements as explained in sections 2.2 and 4.5 as well as ESR measurements as explained in sections 2.2, 2.5 and 5.3.

It has been observed that activating the microwave can change the bias voltage offset. Therefore, the program switches between a bias voltage offset correction value for microwave on and a value for microwave off at every time the microwave is turned on or off.

Additionally, the program implements atom tracking: If a long measurement is performed on a specific location on the surface, like an atom, the tip and the location can move away from each other due to piezo drift. In order to prevent that, atom tracking returns the tip to the original location by measuring the topography in a circle around it. In order to reduce measurement time, it can be desirable to perform multiple bias voltage sweeps per atom tracking, especially if many short bias voltage sweeps are done. Therefore, the number of bias voltage sweeps per atom tracking can be specified. If the magnetic field is changed, there is typically more drift than usual because the eddy current causes Joule heating and thereby thermal expansion. To compensate this, longer atom tracking times can be done after magnetic field changes.

Microwave radiation can cause thermal expansion as well. Since the microwave is directed to the tip, it can specifically cause the tip to expand and crash into the surface. To compensate this, tip crash prevention has been implemented: If the current goes over a threshold, the measurement is stopped to protect the tip. In order to prevent short current noise peaks from stopping the measurement, this is only done if the current threshold is exceeded in more than three subsequent measurement points with a distance of 50 ms which is typically faster than the thermal expansion.

3.5 High Frequency Wiring

Irradiating a high frequency signal into the tunnel junction of the STM is a key requirement for electron spin resonance. The signal transmission to the ultra high vacuum (UHV) of the STM becomes more difficult at higher frequencies due to the skin effect in the metal and the lower permittivity of the dielectric in the cables at higher frequencies. In order to obtain higher Zeeman energies compared to the thermal energy, we resolve the challenge of using higher frequencies than previous STMs. To achieve this, we use a number of parts (see Fig. 3.9).
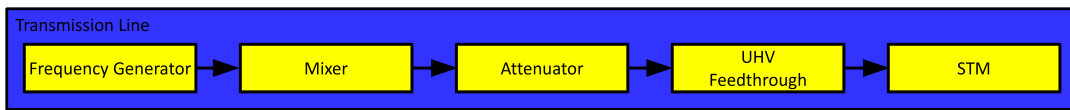

Figure 3.9: Transmission line of all devices where the high frequency signal passes through: The frequency generator is an E8257D PSG Analog Signal Generator from Keysight. The mixer is a WR12 mixer from VDI. The attenuator is a 511 Programmable Attenuator from Millimeter Wave Products Inc. The UHV feedthrough was initially homebuilt and then replaced by the 1.85 mm feedthrough KPC185FFHA from Kawashima Manufacturing Corporation.

The high frequency signal is created by a Keysight E8257D PSG Analog Signal Generator for a frequency range from 250 kHz to 20 GHz. Through a flexible high frequency cable, the signal is transferred to a VDI WR12 mixer for a frequency range from 60 to 90 GHz. This mixer multiplies the frequency of the signal by 6 and amplifies it from 10 dBm to 16 dBm. This corresponds to an increase in power by a factor of approximately 4. Due to the higher frequency of the signal after the mixer, transmission losses become more critical from there on due to the skin effect and the permittivity of the dielectric. At the mixer output, the signal is transmitted through a waveguide to a 511 Programmable Attenuator from Millimeter Wave Products Inc. As the mixer is only calibrated for one specific power value, an attenuator has to be used additionally to vary the signal power. The flexible adjust-

35

ment of the signal attenuation is necessary to compensate different transmission values for different frequencies and thereby keep the signal intensity constant for different frequencies.

After the attenuator, we use a flexible coaxial cable with a silver plated copper shield and conductor with a total outer diameter of $0.047\,\mathrm{in}$. This connects to a hermetically sealed UHV feedthrough. As far as we know, vacuum feedthroughs that are hermetically sealed are not commercially available in our frequency range. Therefore, we have initially built our own feedthrough for which we built our own waveguide. Later, the commercial $1.85\,\mathrm{mm}$ feedthrough KPC185FFHA by Kawashima Manufacturing Corporation was used instead, together with $1\,\mathrm{mm}$ to $1.85\,\mathrm{mm}$ adapters. Even though this feedthrough is only specified for a frequency up to $65\,\mathrm{GHz}$, it improved the transmission and a sufficient signal is obtained even at $100\,\mathrm{GHz}$.

After the vacuum feedthrough in the upper part of the cryostat, the signal is transferred through semirigid cables with a copper jacket and silver-plated copper weld (SPCW) conductor. In the lower, cooled part of the cryostat, the signal is transferred through a superconducting NbTi coaxial cable in order to minimize losses of signal transmission. Additionally, the superconductor prevents heat transport to the helium-3 stage and thereby allows to keep low temperatures. The antenna is connected through a flexible cable of the same type as the one between attenuator and feedthrough. The mechanical flexibility of the cable is required due to the movement of the spring dampers of the STM.

4 Transfer Function Compensation

4.1 Transfer Function Basics

For conducting precise STM experiments with electromagnetic waves such as electron spin resonance, it is of utmost importance to have exact control over frequency and intensity of the signal arriving at the tunnel junction. But sending an electromagnetic high frequency signal through a long transmission line is a nontrivial problem. The longer the line and the higher the frequency, the more difficult a sufficient signal transmission becomes. This makes it especially challenging in our case where we push the upper limit of the frequency range for ESR-STM to 100 GHz. The maximum that has been demonstrated so far is 40 GHz [70]. Additionally, we have to cross a long distance of approximately two meters from the signal generator to the STM. The reason for this is that a liquid helium cryostat is necessary to conduct the experiment at low temperature. One part of the cabling distance goes from the signal generator to the cryostat and the other part goes through the cryostat to the STM. The vacuum feedthrough where the signal is transferred from the outside into the cryostat is especially a point of high signal loss as explained in section 3.5.

The transmission is dampened and distorted depending on the local geometry of all involved parts of the machine. In particular, the impedance has to be matched between all involved parts of the transmission line as good as possible. This can be done until the microwave antenna is reached. However, at the STM, an impedance mismatch is necessarily introduced due to the transi-

tion to the vacuum. Overall, the dependency of the signal transmission on frequency becomes strongly nonlinear.

If the transmission behavior of the high frequency signal through the cabling is known, it can be compensated by varying the input power accordingly. This is especially important for electron spin resonance measurements where a constant microwave intensity is required over a range of frequencies which have different signal transmission. The attenuation that compensates the deviations is done only by our flexible attenuator. The output power of the frequency generator is kept constant to exclude distortions from the mixer which is only calibrated for one power value. This section explains how the irregularities of the transmission line can be compensated by the attenuator if they are known from a measurement. The following sections will show a variety of different techniques to measure the microwave transmission.

In general, the effect of the transmission line on an input signal $s_{\text{in}}(t)$ that depends on time t can be described by an operator $\tilde{T}$:

$$s_{\text{T}}(t) = \tilde{T} s_{\text{in}}(t) \tag{4.1}$$

where $s_{\text{T}}(t)$ is the signal that arrives at the tunnel junction. In the most general case, the operator can be any $\tilde{T} \in L^1(\mathbb{R})^{L^1(\mathbb{R})}$ where $L^1(\mathbb{R})$ is the set of integrable functions from $\mathbb{R}$ to $\mathbb{R}$ with limited 1-norm. It is reasonable to assume that $\tilde{T}$ is a linear operator. As $\tilde{T}$ lies in an infinite-dimensional vector space, it would be very hard to interpolate $\tilde{T}$ based on a finite number of measurement points. By a Fourier transform $\mathcal{F}$ and back transform $\mathcal{F}^{-1}$, $\tilde{T}$ can be simplified to a scalar function $T(\nu)$ that depends only on frequency ν, the so called transfer function T:

$$s_{\text{T}}(t) = \left(\mathcal{F}^{-1}(T(\nu) \mathcal{F} s_{\text{in}}) \right)(t). \tag{4.2}$$

Inverting the whole operator yields

$$\left(\mathcal{F}^{-1}(T(\nu)^{-1} \mathcal{F} s_{\text{T}}) \right)(t) = s_{\text{in}}(t). \tag{4.3}$$

This equation defines which signal s_{in} has to be applied in order to obtain a desired signal s_{T} at the tunnel junction. Receiving a

certain tunnel junction signal requires that the transfer function $T(\nu)$ is known from a measurement. For such a measurement, it is enough to measure the tunnel junction signal intensity over a range of different input frequencies. The transfer function can then be interpolated between the frequency points. Obtaining the tunnel junction signal intensity is the difficult part of the measurement as it is not directly accessible. Different ways to gain indirect access to it will be discussed in the next sections.

In practice, there is the problem that the inversion from (4.2) to (4.3) is not necessarily well defined: If $T(\nu) = 0$ for some frequencies, $T(\nu)^{-1}$ would have to be infinite. If the transmission line is opaque for some frequencies, this cannot be compensated by applying an infinite input signal. Typically, this can be the case for very low frequencies, very high frequencies and a few frequency points in between. Ignoring this problem would cause deviations between the desired and the obtained signal at the tunnel junction.

There are two ways to solve the problem: Firstly, one can choose the desired tunnel junction signal such that it does not include frequencies with zero transmission. Secondly, one can use equation (4.2) instead of (4.3) and optimize s_in such that the distance between the resulting s_T and the desired s_T is minimized. To determine this distance, a metric on the signal function space must be defined, for example as a norm of the difference. As our input signal is usually harmonic, we can usually use the first solution.

By transforming the transfer function to a logarithmic scale with respect to power, the attenuation becomes an addition:

$$16\,\text{dBm} - A_\text{Att} + A_\text{Transf} = D. \tag{4.4}$$

$16\,\text{dBm}$ is the power at the mixer output. A_Att is the attenuation of our flexible attenuator on a logarithmic scale with respect to power with $0\,\text{dB} \leq A_\text{Att} \leq 70\,\text{dB}$. A_Transf is the transfer function attenuation with respect to power and is typically negative. D is the absolute power arriving at the tunnel junction on a dBm scale.

The units of A_Att and A_Transf are dB because they denote relative attenuations.

$$D = 10\,\text{dBm} \cdot \log_{10}\left(\frac{P_\text{T}}{P_\text{ref}}\right) = 10\,\text{dBm} \cdot \log_{10}\left(\frac{V_\text{AC}^2}{2 \cdot RP_\text{ref}}\right) \quad (4.5)$$

$P_\text{T} = \frac{V_\text{AC}^2}{2R}$ is the power arriving at the tunnel junction. The factor $\frac{1}{2}$ is the square of the factor $\frac{\sqrt{2}}{2}$ to translate between effective voltage and the voltage amplitude V_AC. $P_\text{ref} = 1\,\text{mW}$ is the reference power of the dBm scale. $R = 50\,\Omega$ is the line impedance. The voltage amplitude V_AC that arrives at the tunnel junction is

$$V_\text{AC} = 1\,\text{V} \cdot 10^{\frac{A_\text{Transf} - A_\text{Att} + 6\,\text{dBm}}{20\,\text{dBm}}}. \quad (4.6)$$

If a certain value V_AC has been measured at a certain attenuator setting A_Att, the transfer function attenuation at the respective frequency can be determined as

$$A_\text{Transf} = A_\text{Att} - 6\,\text{dB} + 20\,\text{dB} \cdot \log_{10}\left(\frac{V_\text{AC}}{1\,\text{V}}\right). \quad (4.7)$$

The known transfer function attenuation A_Transf can then be used to obtain the desired V_AC by applying the attenuation

$$A_\text{Att} = A_\text{Transf} + 6\,\text{dB} - 20\,\text{dB} \cdot \log_{10}\left(\frac{V_\text{AC}}{1\,\text{V}}\right). \quad (4.8)$$

4.2 Measurement by Tien-Gordon-Effect

It has been shown that the signal arriving at the tunnel junction can be measured by detecting plasmonic light emitted from the junction [29]. This requires a way to directly measure the photons emitted from the junction, for example by using an avalanche single photon counting diode. As this is not available in most STMs including ours, a different method has to be found. The most common alternative way to gain access to the junction signal is by exploiting nonlinearities in the current I in dependency of voltage V_DC. Superconductor-insulator-superconductor (SIS)
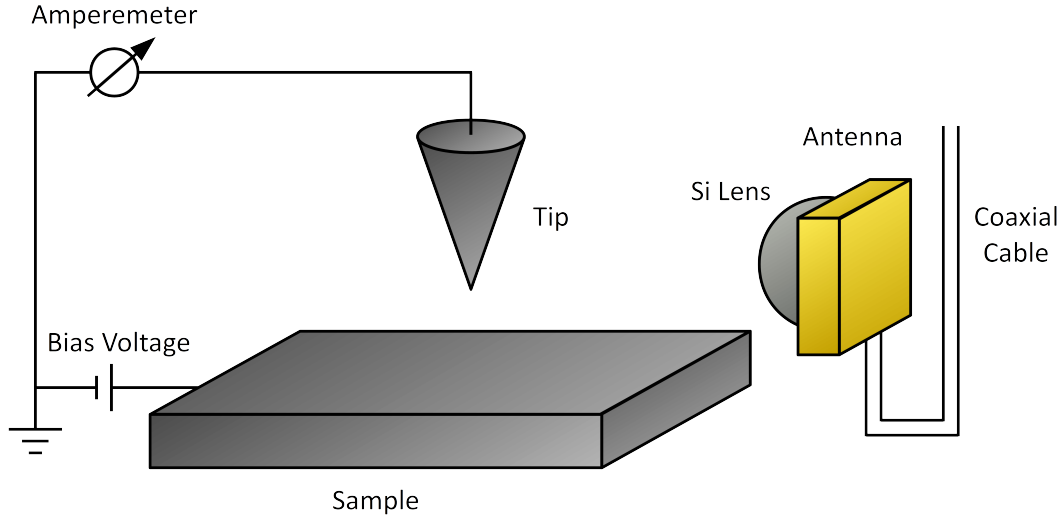
Figure 4.1: STM with external antenna: A hyperhemispheric Si lens is focussing the antenna radiation towards the tunnel junction. The inner and outer conductor of the coaxial cable powering the antenna are both connected to different parts of the antenna geometry.

tunnel junctions are a prominent example for showing such non-linearities. Our first system is an SIS junction between a V(100) surface and a vanadium tip. Vanadium is a type II superconductor with $T_\mathrm{C} = 5.4\,\mathrm{K}$ [81]. Below this temperature, it is energetically favorable for electrons to form Cooper pairs. Only if a voltage $|V| \geq (\Delta_\mathrm{t} + \Delta_\mathrm{s})/e$ is applied between tip and sample, there is a jump in tunneling current I. Here, Δ_t is the superconducting gap parameter of the tip and Δ_s of the sample. The applied voltage effectively shifts the tip and sample densities of states against each other, creating an overlap at sufficient voltage. Above this voltage threshold, the current continues affine-linearly in voltage. In the derivative of the current with respect to bias voltage $\mathrm{d}I/\mathrm{d}V_\mathrm{DC}$, this current jump shows up as coherence peak. The coherence peak at positive bias voltage is symmetric to the one at negative bias voltage.

The tunnel junction can be irradiated by a harmonic high frequency radiation from our antenna. ω is the angular frequency of the radiation. V_AC is the voltage amplitude of the radiation that

arrives at the tunnel junction. The input power of the frequency generator is known. Therefore, determining V_AC, yields the transfer function value at ω. If such a harmonic signal arrives at the tunnel junction, the whole $\mathrm{d}I/\mathrm{d}V_\mathrm{DC}$ becomes a sum of shifted versions of itself as described by the Tien-Gordon equation [20, 65, 75]:

$$I_q\left(V_\mathrm{DC}, V_\mathrm{AC}\right) = \sum_{k=-\infty}^{\infty} \mathrm{J}_k^2\left(\frac{qV_\mathrm{AC}}{\hbar\omega}\right) I\left(V_\mathrm{DC} - \frac{k\hbar\omega}{q}\right). \qquad (4.9)$$

Here, $\hbar$ is Planck's constant and J_k is the k-th Bessel function of the first kind. For the case of quasiparticle tunneling considered here, the charge is the elementary charge, $q = e$. For Cooper pair tunneling that happens at voltages with smaller absolute value, $q = 2e$ applies. The energy difference between the replica is an integer multiple of the relation between frequency $\hbar\omega$ and charge q. Even though the whole $\mathrm{d}I/\mathrm{d}V_\mathrm{DC}$ is replicated, the replica of the coherence peaks are most notable. Squared Bessel functions describe how the replica peak height depends on the relation between the microwaves' electric field and frequency. Figure 4.2 shows the $\mathrm{d}I/\mathrm{d}V$ for different microwave amplitudes V_AC. If a certain microwave power is applied at the input of the transmission line, the measured $\mathrm{d}I/\mathrm{d}V$ can be fitted precisely by using the Tien-Gordon equation with V_AC as a fit parameter (see Fig. 4.2). This requires a reference measurement without microwave to obtain $I(V_\mathrm{DC})$ which enters the Tien-Gordon equation (4.9). Due to the high accuracy of the fit, the obtained fit parameter V_AC is very reliable.

A measurement of the $\mathrm{d}I/\mathrm{d}V$ in dependency of V_DC and V_AC shows how the replica peak heights and positions vary with microwave power (see Fig. 4.3).

Measuring $\mathrm{d}I/\mathrm{d}V$ for multiple different frequencies ν (see Fig. 4.4) grants access to the transfer function (see Fig. 4.5). For that, it is sufficient to measure $\mathrm{d}I/\mathrm{d}V$ in dependency of V_DC at any one microwave amplitude V_AC for each frequency and use one reference measurement without microwave for all frequencies. In between the measured frequency points, the transfer function is interpo-
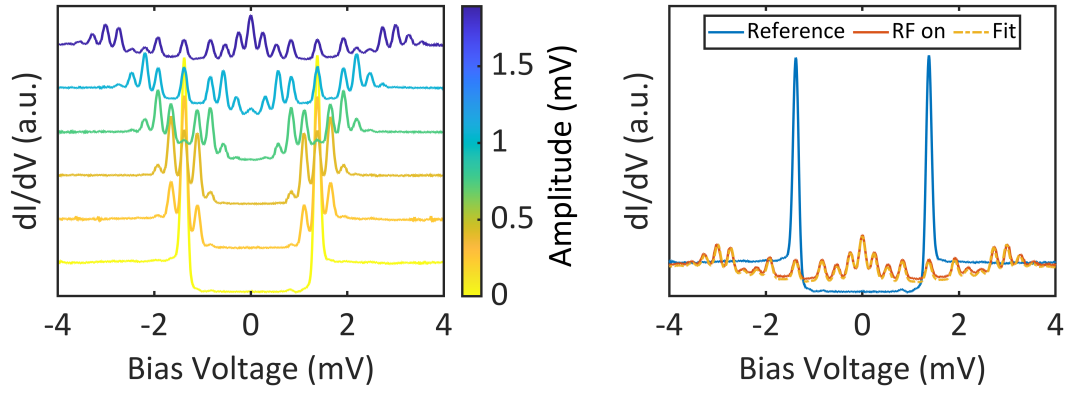
Figure 4.2: Left: dI/dV in dependency of V_{DC} for different values of V_{AC}; Right: dI/dV in dependency of V_{DC} without microwave (reference) and with microwave (RF On). The fit matches the data well and allows for the extraction of V_{AC}.
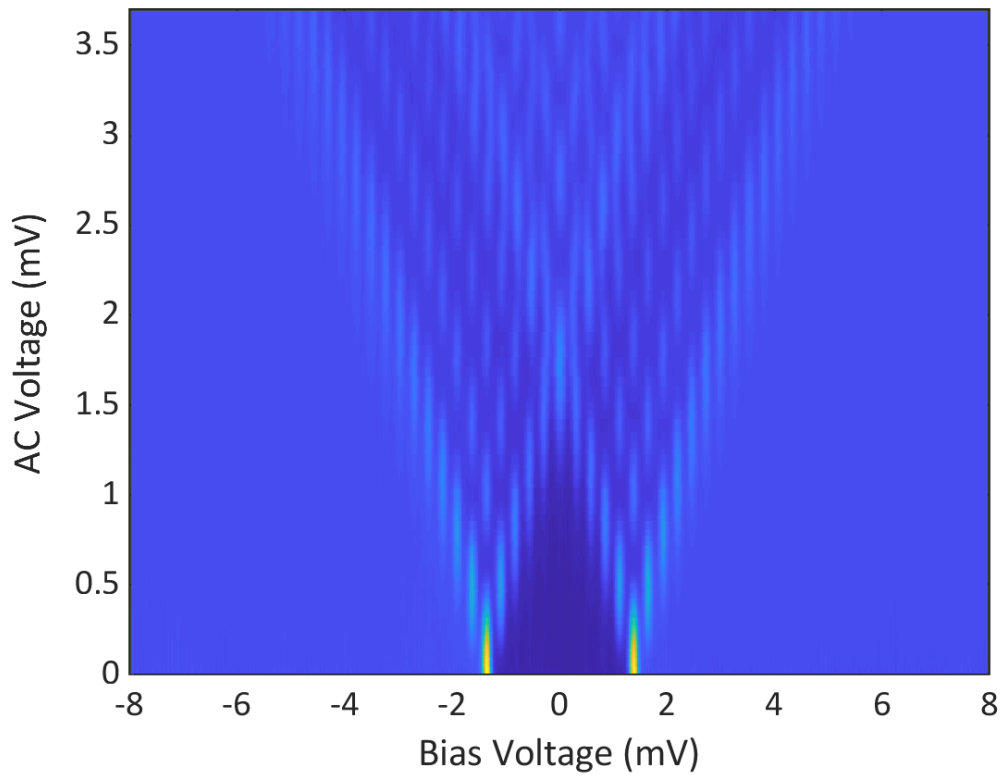

Figure 4.3: dI/dV in dependency of V_{DC} and V_{AC}: The coherence peaks are increasingly split with increasing V_{AC}.
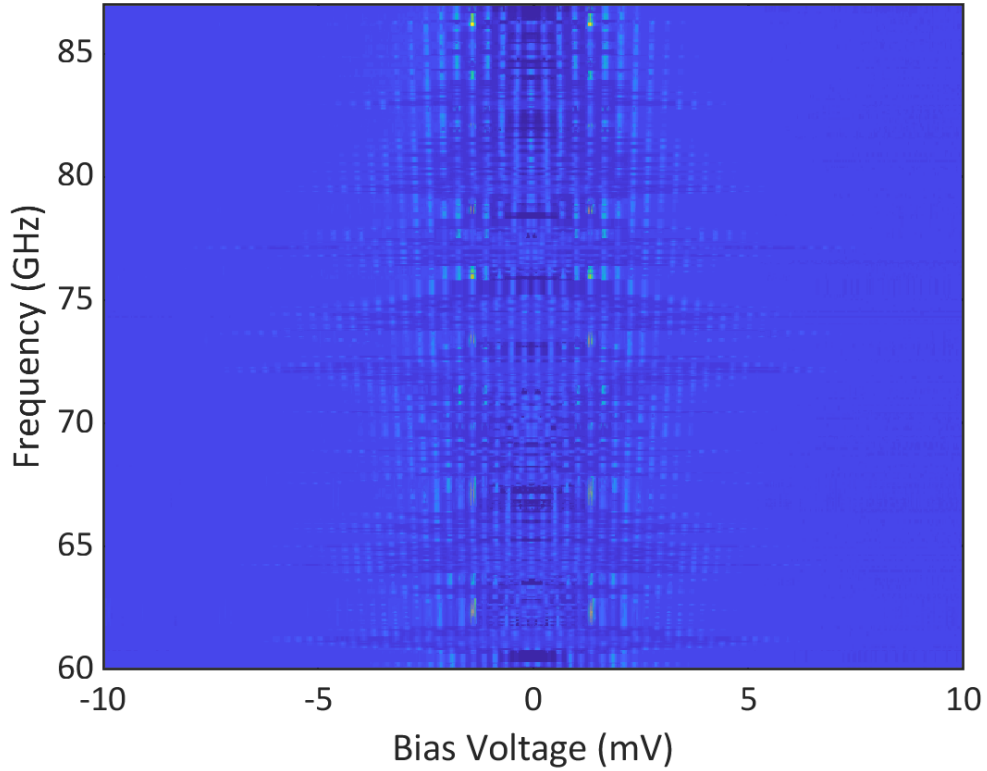
Figure 4.4: dI/dV in dependency of V_{DC} and frequency ν: It can be seen that the dependency in ν is very irregular.

lated linearly on a logarithmic scale with respect to microwave power according to equations (4.4) and (4.5). Outside of the measured frequency range, the transfer function cannot be known reliably. The measurement program continues it as a constant equal to the closest known value and reports an error if transfer function compensation should be used outside of the known range.

Even though the Tien-Gordon equation (4.9) allows for very good fits, finding the right value for V_{AC} can be a challenge for some fitting algorithms: The deviation between fit function and data has many local minima. Reducing the fit parameter V_{AC} by certain amounts eliminates the outer coherence peak replica while the inner ones may still fit well. The same is true for adding additional outer coherence peak replica by increasing V_{AC}. Therefore,
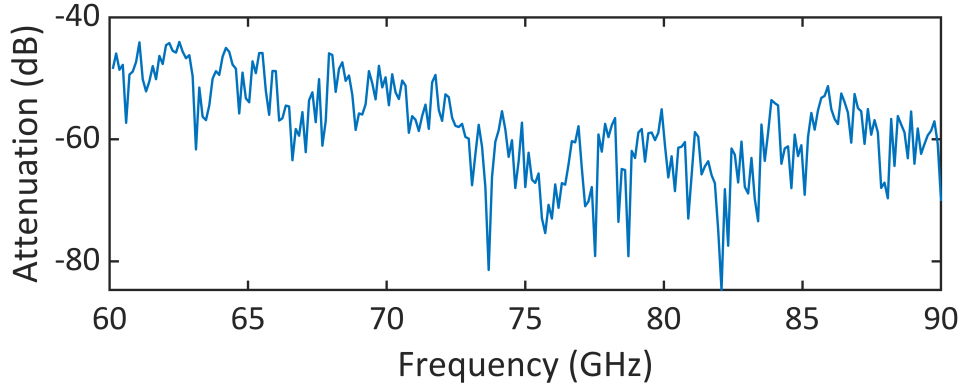
44

Figure 4.5: Transfer function on a logarithmic scale with respect to microwave power in dependency of frequency ν: It can be seen that the power depends strongly nonlinearly on the frequency and tends to be smaller at higher frequency. Still, there is a significant signal throughout the whole frequency range except for few singular outlier frequencies.

care must be taken that the fit algorithm finds the correct local minimum.

4.3 Efficient Peak Height Method

Measuring a full dI/dV graph for each frequency takes about 30 hours with a frequency resolution of 12 MHz. Within this time, the whole helium condensation evaporates due to the microwave heat and has to be recondensed. In order to maximize the frequency resolution per measurement time, the bias voltage resolution has to be minimized. Few bias voltage points are enough to reliably fit the Tien-Gordon equation for each frequency if a more advanced approach is used.

The only effect of the transfer function is a stretching of Fig. 4.3 in the vertical direction. This can be determined much more efficiently: It is enough to measure a single point per frequency if and only if this point is within the area marked in red in Fig. 4.6. At higher microwave intensities, the Tien-Gordon equation cannot be solved for V_{AC} because the sum of squared Bessel functions of the

45

first kind is not injective. It produces the same coherence peak heights for different microwave amplitudes V_{AC} as can be seen in Fig. 4.6.
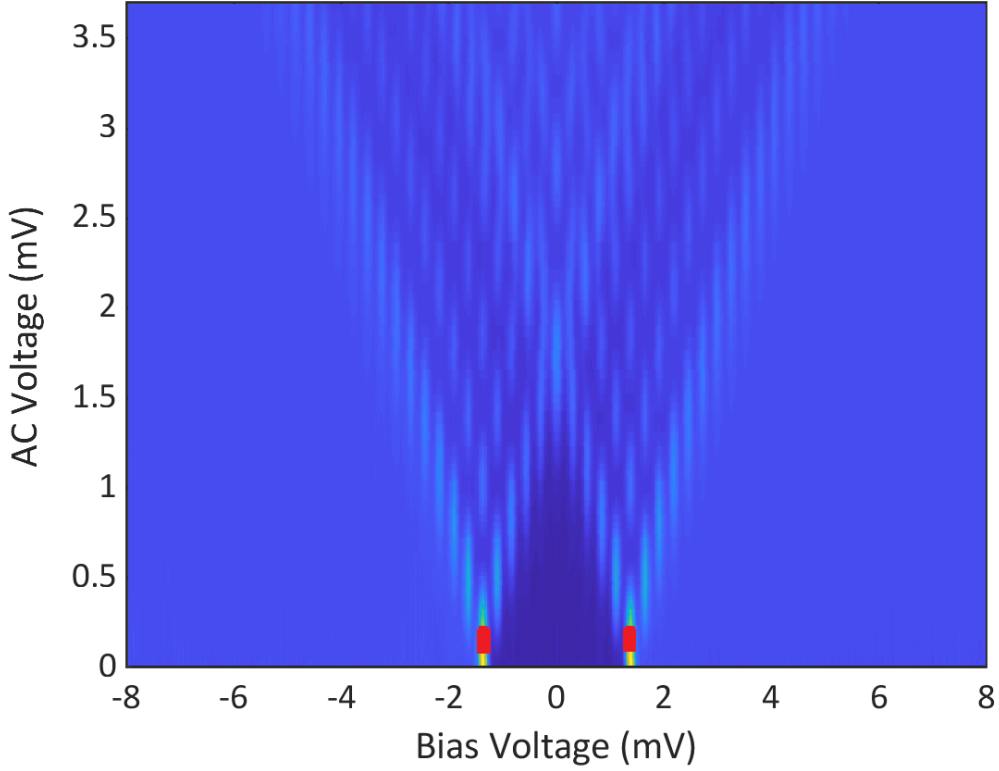

Figure 4.6: $\mathrm{d}I/\mathrm{d}V$ in dependency of V_{DC} and V_{AC}: The injectivity area of the sum of squared Bessel functions is marked in red.

If a certain peak height value has been measured, it is important to check if it is within the injective range. With increasing V_{AC}, the number of peak replica increases but their maximum height decreases. The measured value is for sure within the injective range if and only if it is larger than the second maximum of the sum of squared Bessel functions. This is equivalent to a Bessel argument $\frac{qV_{\mathrm{AC}}}{\hbar\omega} < \mathrm{j}_{1,1} \approx 3.832$ where $\mathrm{j}_{1,1}$ is the second root of J_1, the first local minimum of J_0 or the second local maximum of J_0^2. If the measured peak height is out of the injective range, the measurement program varies V_{AC} until it is inside. A good microwave

amplitude value to stay in the desired Bessel function range for the antenna frequency range from 60 to 90 GHz is $V_{\text{AC}} = 300\,\mu V$. This low value has the additional advantage of lower heat-up and therefore longer holding time of the He condensation compared to measuring full voltage sweeps. V_{AC} can be determined by searching the root of the Tien-Gordon equation minus the measured value $\frac{\partial I}{\partial V_{\text{DC}}}\left(V_{\text{DC}}, V_{\text{AC}}, \nu\right)$ which is defined as the function U in dependency of V_{AC}:

$$U(V_{\text{AC}}) := \sum_{k=-\infty}^{\infty} \mathrm{J}_k^2\left(\frac{qV_{\text{AC}}}{\hbar\omega}\right) \frac{\partial I}{\partial V_{\text{DC}}}\left(V_{\text{DC}} - \frac{k\hbar\omega}{q}\right) -$$
$$- \frac{\partial I}{\partial V_{\text{DC}}}(V_{\text{DC}}, V_{\text{AC}}, \nu) = 0 \quad (4.10)$$

The nonlinear equation (4.10) can be solved by applying Newton's method where $V_{\text{AC}}^{(n)}$ denotes the result of the n-th step of the iteration:

$$V_{\text{AC}}^{(0)} = 300\,\mu V, \qquad (4.11)$$

$$V_{\text{AC}}^{(n+1)} = V_{\text{AC}}^{(n)} - U(V_{\text{AC}}^{(n)})/\frac{\mathrm{d}U(V_{\text{AC}}^{(n)})}{\mathrm{d}V_{\text{AC}}^{(n)}} = V_{\text{AC}}^{(n)} -$$
$$- \frac{\hbar\omega\left(\sum_{k=-\infty}^{\infty} \mathrm{J}_k^2\left(\frac{qV_{\text{AC}}^{(n)}}{\hbar\omega}\right)\frac{\partial I}{\partial V_{\text{DC}}}\left(V_{\text{DC}} - \frac{k\hbar\omega}{q}\right) - \frac{\partial I}{\partial V_{\text{DC}}}(V_{\text{DC}}, V_{\text{AC}}, \nu)\right)}{q\sum_{k=-\infty}^{\infty}\left(\mathrm{J}_k \cdot (\mathrm{J}_{k-1} - \mathrm{J}_{k+1})\right)\left(\frac{qV_{\text{AC}}^{(n)}}{\hbar\omega}\right)\frac{\partial I}{\partial V_{\text{DC}}}\left(V_{\text{DC}} - \frac{k\hbar\omega}{q}\right)}$$
$$(4.12)$$

with $q = e$ for our case of quasiparticle tunneling. The calculation still requires measuring a reference bias voltage sweep $\frac{\partial I}{\partial V_{\text{DC}}}(V_{\text{DC}})$ without microwave and with high bias voltage resolution. $\frac{\partial I}{\partial V_{\text{DC}}}(V_{\text{DC}}, V_{\text{AC}}, \nu)$ is the measured peak height with microwave.

The calculation must be done during the measurement by the measurement program because the next measurement parameters depend on the previous ones. Calculating many Bessel functions is computationally expensive. In order to save computation time during the measurement, the number of Bessel function calculations is reduced by using $J_{-k} = (-1)^k J_k \forall k \in \mathbb{Z}$ and the results of already calculated Bessel functions are reused as much as possible. While equation (4.12) is a very simple formulation for analytical calculation, the algorithmically more efficient formulation is

$$V_{\mathrm{AC}}^{(n+1)} = V_{\mathrm{AC}}^{(n)} - \hbar\omega \left(J_0^2 \left(\frac{qV_{\mathrm{AC}}^{(n)}}{\hbar\omega} \right) \frac{\partial I}{\partial V_{\mathrm{DC}}} (V_{\mathrm{DC}}) + \right.$$

$$+ \sum_{k=1}^{\infty} J_k^2 \left(\frac{qV_{\mathrm{AC}}^{(n)}}{\hbar\omega} \right) \left(\frac{\partial I}{\partial V_{\mathrm{DC}}} \left(V_{\mathrm{DC}} - \frac{k\hbar\omega}{q} \right) + \frac{\partial I}{\partial V_{\mathrm{DC}}} \left(V_{\mathrm{DC}} + \frac{k\hbar\omega}{q} \right) \right) -$$

$$\left. - \frac{\partial I}{\partial V_{\mathrm{DC}}} (V_{\mathrm{DC}}, V_{\mathrm{AC}}, \nu) \right) \bigg/ \left(q \left((J_0 \cdot (J_{-1} - J_1)) \left(\frac{qV_{\mathrm{AC}}^{(n)}}{\hbar\omega} \right) \frac{\partial I}{\partial V_{\mathrm{DC}}} (V_{\mathrm{DC}}) + \right. \right.$$

$$+ \sum_{k=1}^{\infty} (J_k \cdot (J_{k-1} - J_{k+1})) \left(\frac{qV_{\mathrm{AC}}^{(n)}}{\hbar\omega} \right) \cdot$$

$$\cdot \left. \left. \left(\frac{\partial I}{\partial V_{\mathrm{DC}}} \left(V_{\mathrm{DC}} - \frac{k\hbar\omega}{q} \right) + \frac{\partial I}{\partial V_{\mathrm{DC}}} \left(V_{\mathrm{DC}} + \frac{k\hbar\omega}{q} \right) \right) \right) \right). \quad (4.13)$$

Compared to full bias voltage sweeps, the peak height method improves the relation between frequency resolution and measurement time by a factor of approximately 300.

If the coherence peak height is measured at a bias voltage that deviates slightly from the position of the peak maximum, the peak height is underestimated by the measurement. This causes an overestimation of the microwave amplitude because for small microwave amplitudes, the sum of squared Bessel functions is decreasing with increasing microwave amplitude. Therefore, transfer function deviations can be caused by small time-dependent bias voltage offsets during the measurement. While a fast transfer function measurement is nonetheless possible, accuracy can be

increased by solving this problem as follows: Measuring dI/dV for multiple bias voltage points around the coherence peak for each frequency allows the extraction of the exact coherence peak maximum by a Lorentzian peak fit for each frequency. This still requires much less bias voltage points than a full bias voltage sweep. For high accuracy, we use up to nine bias voltage points per frequency. With so few points at a different V_{AC}, a full Tien-Gordon fit would not be reliable due to the local minima problem discussed in the previous section. For the peak height method, however, this problem does not exist due to being in the injective range because sufficiently small AC voltage amplitudes are used.
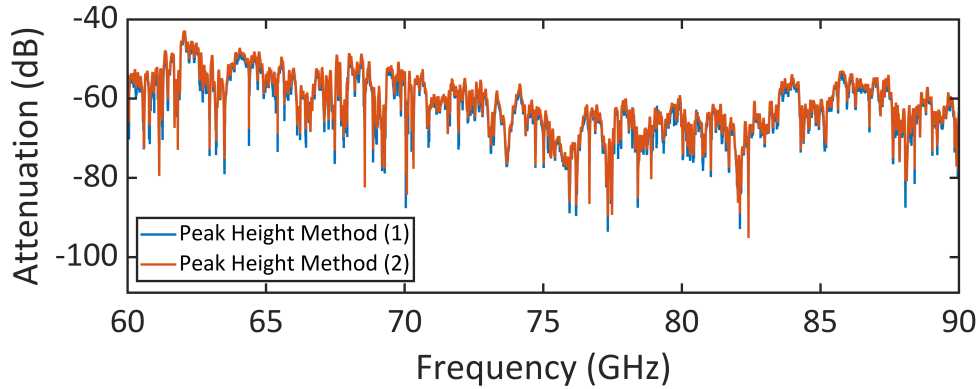

Figure 4.7: Transfer function on a logarithmic scale with respect to microwave power in dependency of frequency ν: The two measurements (1) and (2) are very similar because they were performed on consecutive days.

The transfer function measurement via the peak height method is reproducible as shown by Fig. 4.7. However, the transfer function varies over times of multiple weeks (see Fig. 4.8). We may speculate that this is due to thermal expansion and contraction due to He evaporation and refilling of the cryostat as well as liquid condensation and evaporation in the dielectric of the high frequency cabling.

In order to increase accuracy additionally, an automatized feedback technique has been implemented that applies the compensation of the previous transfer function measurement and measures

it again until a set accuracy or the maximum iteration number is reached for every frequency. This is equivalent to multiple subsequent measurements where inaccurate measurement points are measured more often.
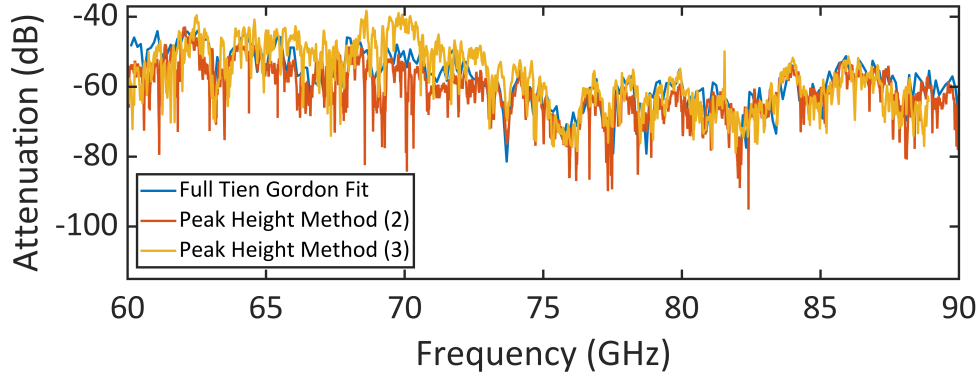

Figure 4.8: Transfer functions on a logarithmic scale with respect to microwave power in dependency of frequency ν: The full Tien Gordon fit is in good agreement with measurement (2) with the peak height method. This means that the peak height method is correct. The deviations are mostly due to one month lying in between the measurements. Measurement (3) shows bigger deviations because it was measured 4 months after (2). This shows that the transfer function changes more in dependency of time than due to different measurement methods. We may speculate that the time dependent changes are due to thermal stress as well as condensed liquid in the dielectric of the high frequency cabling, caused by refilling liquid helium. (3) has by far not as many negative outliers as (2) because it was measured with the more advanced error correction protocol.

Additionally, an error correction protocol has been introduced. The measurement program tracks different errors that can happen during measurement and analysis. Here, the term "error" does not refer to any kind of statistical deviation between multiple measurement points but to a problem that is noticed for a single measurement point in frequency. Measurement points with errors are measured again up to the maximum iteration number. If there are measurements without errors for a frequency, only those are used in the averaging to determine mean value and standard deviation. The following errors are distinguished:

Error Code	Error Description
1	Maximum at bias voltage edge
2	Reference maximum at bias voltage edge
4	Maximum out of injecticve range
8	Fit does not converge
16	AC voltage negative
32	Fit result bad
64	Bessel argument too big for first solution
128	Attenuation negative
256	Attenuation greater than $70\,\mathrm{dB}$
512	Peak fit function loading error
1024	Peak fitting error
2048	Reference peak fit function loading error
4096	Reference peak fitting error

The error code sum is the sum of error codes. Since the error codes are powers of 2, the sum includes the total information of whether every single error occured. The error code sum is stored for every measurement point.

The use of the error correction protocol drastically reduces the amount of negative outliers in the transfer function (see Fig. 4.8). By combining feedback averaging with the error correction protocol, the transfer function was compensated such that a relative standard deviation of the microwave voltage amplitude from the desired value of $4.5\,\%$ has been reached.

4.4 Measurement by Inelastic Step

In order to do ESR-STM on an established system, namely an MgO bilayer on Ag(100) probed with a PtIr tip [88], a different transfer function technique is needed: As this is no longer a superconductor, the coherence peaks can no longer serve as a nonlinearity. At first, it has been tried to apply the peak height method described in the last section to the intrinsic MgO peak at $2.4\,\mathrm{V}$ [21, 24]. However, this peak is too broad to be meaningfully

changed by the small microwave amplitude that is required to be within the injective range. Therefore, the measurement method has to be changed for this case. By applying the Tien-Gordon equation (4.9) to the dI/dV step at a TiH molecule on the surface (see Fig. 4.9), V_{AC} and therefore the transfer function can be extracted nicely. This requires a reference measurement without microwave. With increasing V_{AC}, the step becomes less sharp. As no discrete peak replica become apparent, there are no problems with local minima or injectivity in the fit. In order to increase efficiency, it is enough to measure only a few bias voltage points per frequency. However, the reference bias voltage sweep without microwave must have a high bias voltage resolution.
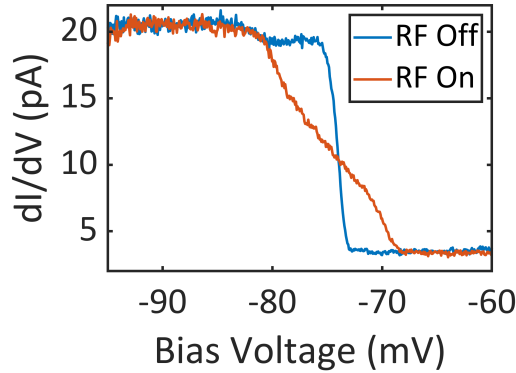

Figure 4.9: dI/dV Step: The signal without radio frequency (RF Off) is changed by activating the microwave radiation (RF On). By applying the Tien-Gordon equation (4.9) on the data without radio frequency, the data with radio frequency can be fitted with the microwave amplitude as a fit parameter. The shown data is raw data without normalization of the vertical axis.

Within the calculation of the fit function, high Tien-Gordon orders are needed. Since the bias voltage shift increases for higher order Tien-Gordon terms, reference values with microwave off have to be known for a wide bias voltage range. Even if the reference is measured over a wide bias voltage range, the shifts will eventually be out of the reference bias voltage range for high Tien-Gordon orders. Increasing the bias voltage range of the reference mea-

surement sufficiently is suboptimal because it would reduce the relation between bias voltage resolution and measurement time and would require changing the voltage divider which would potentially introduce offsets in $\mathrm{d}I/\mathrm{d}V$ and bias voltage. Instead, the $\mathrm{d}I/\mathrm{d}V$ signal is extrapolated if the shifted bias voltage within the Tien-Gordon equation (4.9) is out of the reference range. This is possible because there are no irregular features away from the peak. The major challenge is to consider noise in the data. Multiple extrapolation functions have been developed. The one that matches the data best is a continuation as a linear fit of the outer 5 % of the reference measurement for the positive and negative bias voltage edge, respectively.

4.5 Lock-In Calibration

In an attempt to improve the relation between transfer function accuracy and measurement time, a lock-in scheme [57] [70] has been implemented. The scheme consists of four steps: First of all, a reference sweep $\mathrm{d}I/\mathrm{d}V\,(V_{\mathrm{DC}})$ without microwave is measured with high bias voltage resolution. Secondly, for one microwave frequency and one microwave input power, a sweep $\mathrm{d}I/\mathrm{d}V\,(V_{\mathrm{DC}})$ is measured. By applying the Tien-Gordon equation (4.9) on the reference sweep, the microwave sweep can be fitted with V_{AC} as a fit parameter. From this, the transfer function is determined by equation (4.7) for that one reference frequency point only. Thirdly, chopping cycles of microwave on and microwave off of equal length are applied. Here, the microwave frequency is the reference frequency and the chopping frequency is about $80\,\mathrm{Hz}$. The difference between the $\mathrm{d}I/\mathrm{d}V$ signal for microwave on and microwave off is measured with a lock-in amplifier with respect to the chopping frequency at one bias voltage where there is a big difference between microwave on and off. A good bias voltage is usually slightly away from the middle of the step. This lock-in signal I_{LI} is measured in dependency of V_{AC}. This is the so called calibration curve. As the

transfer function is known for the reference frequency, it is known which input power has to be applied to reach certain values of V_{AC}. It is reasonable to assume that the calibration curve is independent of frequency. Finally, the lock-in signal is measured in dependency of microwave frequency for one microwave power while microwave chopping is active. Knowing only one point in power for each microwave frequency is enough to determine the transfer function for each frequency point because the full calibration curve is known.

In contrast to the published realizations of this scheme [57] [70], we use the full Tien-Gordon equation (4.9) instead of the arcsine convolution approximation to fit to the step. This is the more general solution for high frequency which we use because our frequency range is higher than the previous implementations. Additionally, we use more general fit functions to fit the calibration curve that translates between lock-in signal and microwave amplitude. This is the key to optimizing accuracy. So far, a polynomial of 3rd order was used to translate from the logarithm of the lock-in signal I_{LI} to the logarithm of V_{AC} [57]. Using this fit function causes deviations between fit and data. Our data shows that more general fit functions are needed to fit calibration curves. Polynomials up to 5th order were tried, translating from I_{LI} to V_{AC} and vice versa, on logarithmic and on linear scales. However, this is not enough to fit the very general shapes that calibration curves may have. A very general shape is shown in Fig. 4.10. To obtain good fits, the numbers must be close to 1. Therefore, we standardize I_{LI} to be expressed in units of $10\,\mathrm{pA}$ and V_{AC} in units of $10\,\mathrm{mV}$. As a fit function, we use a smooth cubic spline interpolation.

Smoothing cubic splines must have natural/variational boundary conditions. But only components of even numbered order may appear in the Taylor expansion of $I_{LI}(V_{AC})$ [70]. Therefore, the fit function must go from V_{AC} to I_{LI} rather than the other way round. In order to get V_{AC} from I_{LI}, the fit function must be injective. There is a workaround to get smooth splines with other
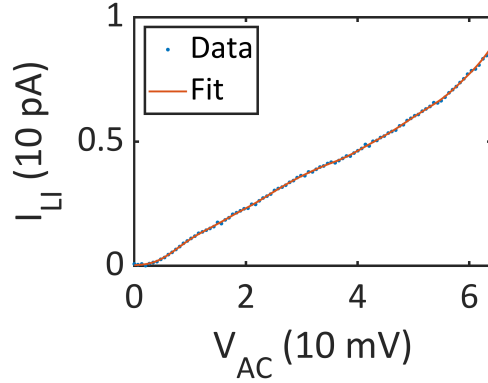
Figure 4.10: The calibration curve shows the lock-in current signal in dependency of microwave amplitude. It was standardized to be calculated in units of $10\,\mathrm{mV}$ and $10\,\mathrm{pA}$ in order to bring the values close to 1 which is important for good fitting. The fit uses a cubic smooth spline interpolation with a smoothing balance parameter of 0.995.

boundary conditions which are not smoothing splines in the strict sense.

Smoothing cubic spline interpolation requires a constant smoothing balance parameter λ in the interval $[0, 1]$. 0 produces a linear fit, 1 an unsmooth cubic spline that overfits the data. If the smoothing balance parameter is too high, it can happen that the fit function is not injective. An algorithm has been developed to reduce the parameter so far that injectivity is guaranteed. It uses the finding that the injectivity of a cubic spline is equivalent to the nonexistence of a spline segment that has a real root of its derivative of single multiplicity within its closed segment range. As long as there is an injectivity violation, the algorithm tries with a new smoothing balance parameter $\lambda_{\mathrm{new}} = \frac{9}{10/\lambda_{\mathrm{old}} - 1}$.

If there are multiple I_{LI} measurement points at the same V_{AC}, the algorithm considers all those data points by combining them into one and increasing its weighting proportionally to the number of measurements.

During the measurement, the tip may drift away from the atom. To compensate that, automated atom tracking in between the

measurement sweeps has been implemented. To further improve precision, the feedback averaging scheme and the error correction protocol are used as described before. This allows us to measure highly accurate transfer functions.

5 First Results in Electron Spin Resonance Spectroscopy

5.1 Decoupling Layers

The content of this chapter is partially published in our paper [18].

Electron spin resonance requires that the particles to be analyzed have unpaired electrons. Only then, their spin states can be excited between the Zeeman levels by an applied microwave. Additionally, spin interactions between the atoms to be studied and the surrounding atoms can disturb the measurement. This is a major challenge if single atoms on a surface are studied, as in electron spin resonance scanning tunneling microscopy (ESR-STM).

Therefore, it is necessary to decouple the spin system from the surface. At the same time, the surface must still be conducting such that a tunneling current can be measured. This can be achieved by spin decoupling layers between a conducting surface and the spin system on top of it. The layer must be thin enough such that a current can tunnel through while also being thick enough to provide sufficient decoupling. An established system that meets these requirements is a double-layer of MgO on Ag(100) [88].

In order to prepare MgO on Ag(100), it is necessary to first prepare clean Ag(100) *in situ* by multiple cycles of Ar ion sputtering and annealing. The annealing temperature is approximately 630 °C. After the last annealing cycle, the Ag sample is not cooled down fully, but only to a temperature of 410 °C. The Mg is preheated to 510 to 520 °C. Then, O_2 is introduced into the vacuum chamber to create an oxygen atmosphere with a partial pressure

of $1 \cdot 10^{-6}$ mbar. The thermal exchange with the inserted oxygen reduces the Ag temperature to approximately 400 °C. If the Ag temperature deviates from 400 °C, the annealing parameters are adjusted such that the Ag temperature is 400 °C. The shutter of the evaporator is opened to evaporate Mg for 15 min in the O_2 atmosphere. This creates islands of MgO double-layers on the Ag surface. Afterwards, the sample is cooled down slowly by ramping down the temperature. The prepared sample is then checked in the STM to see if it exhibits the described desired properties [21, 69].
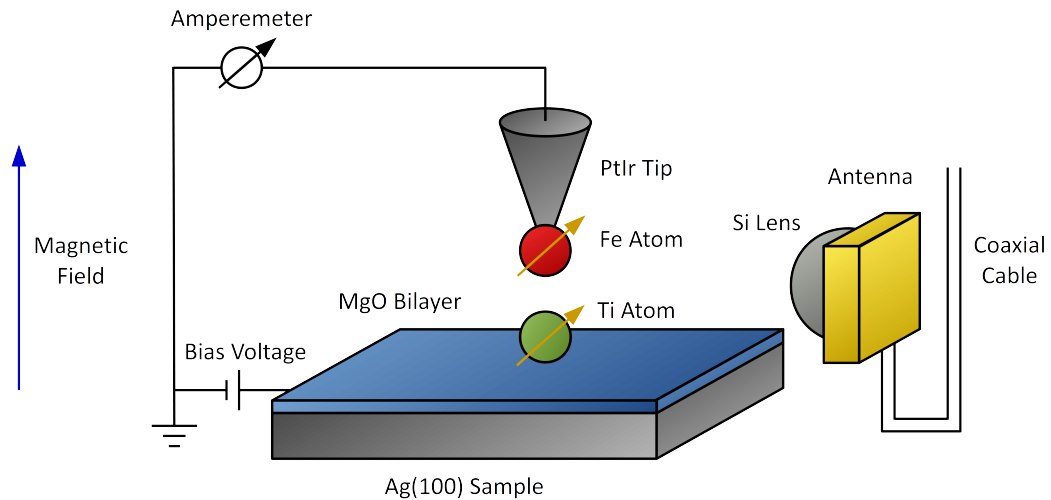
5.2 Spin Systems

Figure 5.1: ESR-STM: The magnetoresistance between an Fe atom at the tip and a TiH molecule on the surface is measured. An MgO bilayer isolates the Ti from the Ag(100) sample. The spin is excited by a high frequency signal from the external antenna.

Ti atoms and Fe atoms are evaporated on the sample. It is important that the sample remains cold during this process so that the atoms do not cluster. Ti atoms most likely form TiH molecules on the sample. It is possible to distinguish topographically and spectroscopically TiH molecules on top of O atoms from the MgO and TiH molecules on top of bridge sites between two O atoms

of the MgO. In the STM, an Fe atom is searched and picked up with the tip. Then, the tip is moved above a Ti atom. An external magnetic field is applied to trigger the Zeeman splitting of the spin energy levels. If an electromagnetic wave is radiated via the antenna, the spin state can be driven if and only if the frequency matches the Zeeman splitting energy. The magnetoresistance, which carries the ESR signal [7], between the two spin systems can be measured in the tunneling current.

5.3 ESR Lock-In Scheme

The spin system excitation causes only a small change in the tunneling magnetoresistance. Therefore, the observation of the ESR signal requires the measurement of small current differences. In order to realize this, an ESR lock-in scheme is implemented [57, 70]. It makes use of a chopping scheme where the antenna radiation is switched on and off. This allows the measurement of the signal difference between microwave on and off. This difference is measured by a lock-in amplifier. We usually use a microwave chopping frequency of 80 Hz. There are the following restrictions for the choice of this value: The chopping frequency must be much smaller than the microwave frequency so that potential time-dependent line shape distortions of the electric field which could happen within few nanoseconds around switching on and off become negligible. More importantly, the chopping frequency must be clearly below the upper cutoff frequency of the transimpedance amplifier of 1 kHz so that the signal modulation is preserved after the transimpedance amplifier. Finally, the chopping frequency must be high enough such that many chopping cycles happen for each measurement point which takes time on the order of seconds. We usually use 80 Hz instead of 100 Hz to avoid higher harmonics of potential residual 50 Hz noise.

The measured time-dependent current signal before lock-in demodulation is $I(t)$. This signal includes a magnetoresistance de-
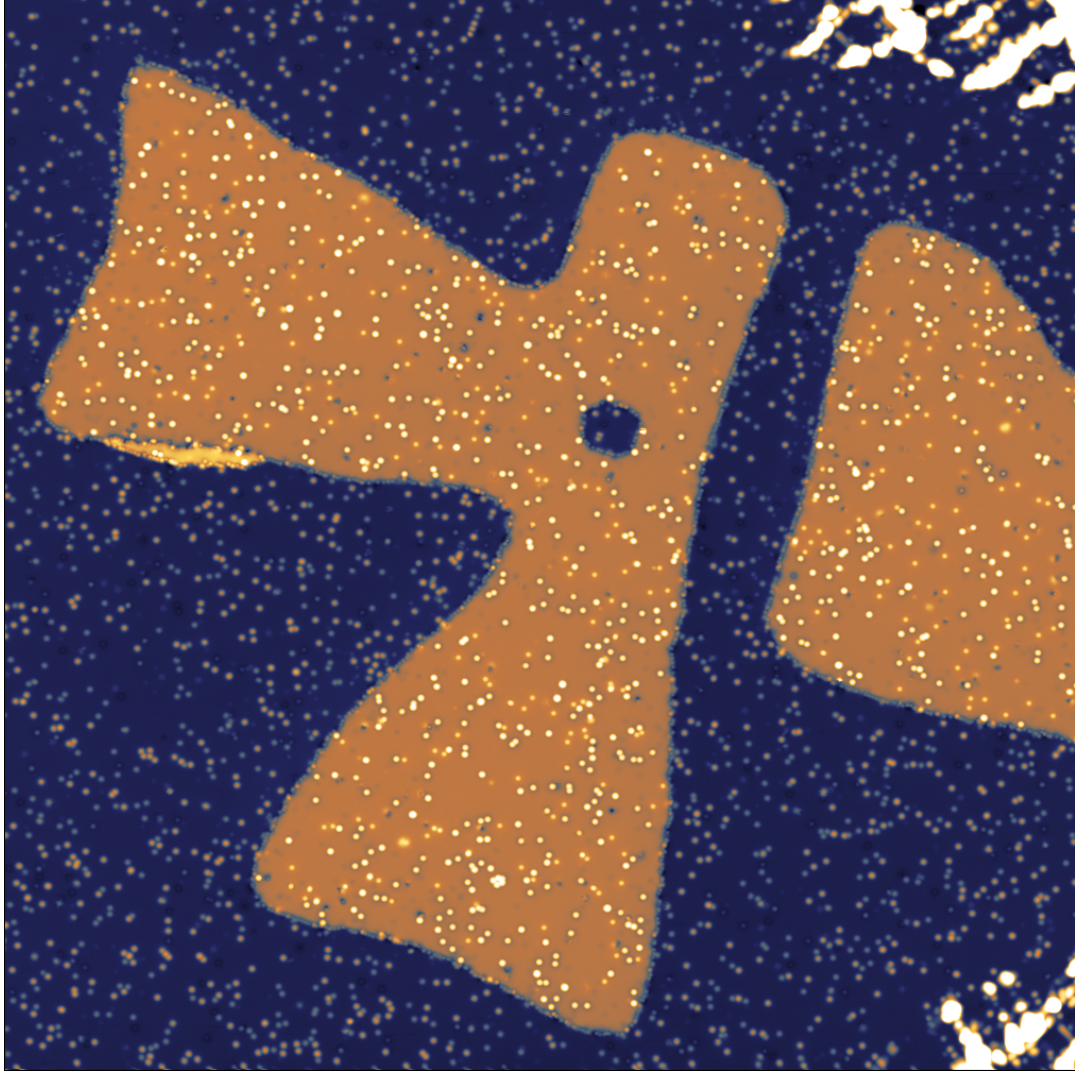
Figure 5.2: The blue area is the bare Ag(100) crystal. The orange area is an atomic double-layer of MgO on top of the Ag. Three species of atoms on top of the surface can be distinguished: 1. Fe atoms, 2. TiH molecules on top of O atoms of the MgO and 3. TiH molecules on top of bridge sites between two O atoms of the MgO.

pendent modulation with the chopping frequency ν_{chop}. The lock-in amplifier outputs two signals X and Y. X can be assumed to be proportional to a time average of $I(t) \cdot \cos(2\pi\nu_{\text{chop}}t - \phi)$ where t is the time and ϕ an arbitrary phase difference. Analogously, Y can be assumed to be proportional to a time average of $I(t) \cdot \sin(2\pi\nu_{\text{chop}}t - \phi)$. The unknown phase difference between
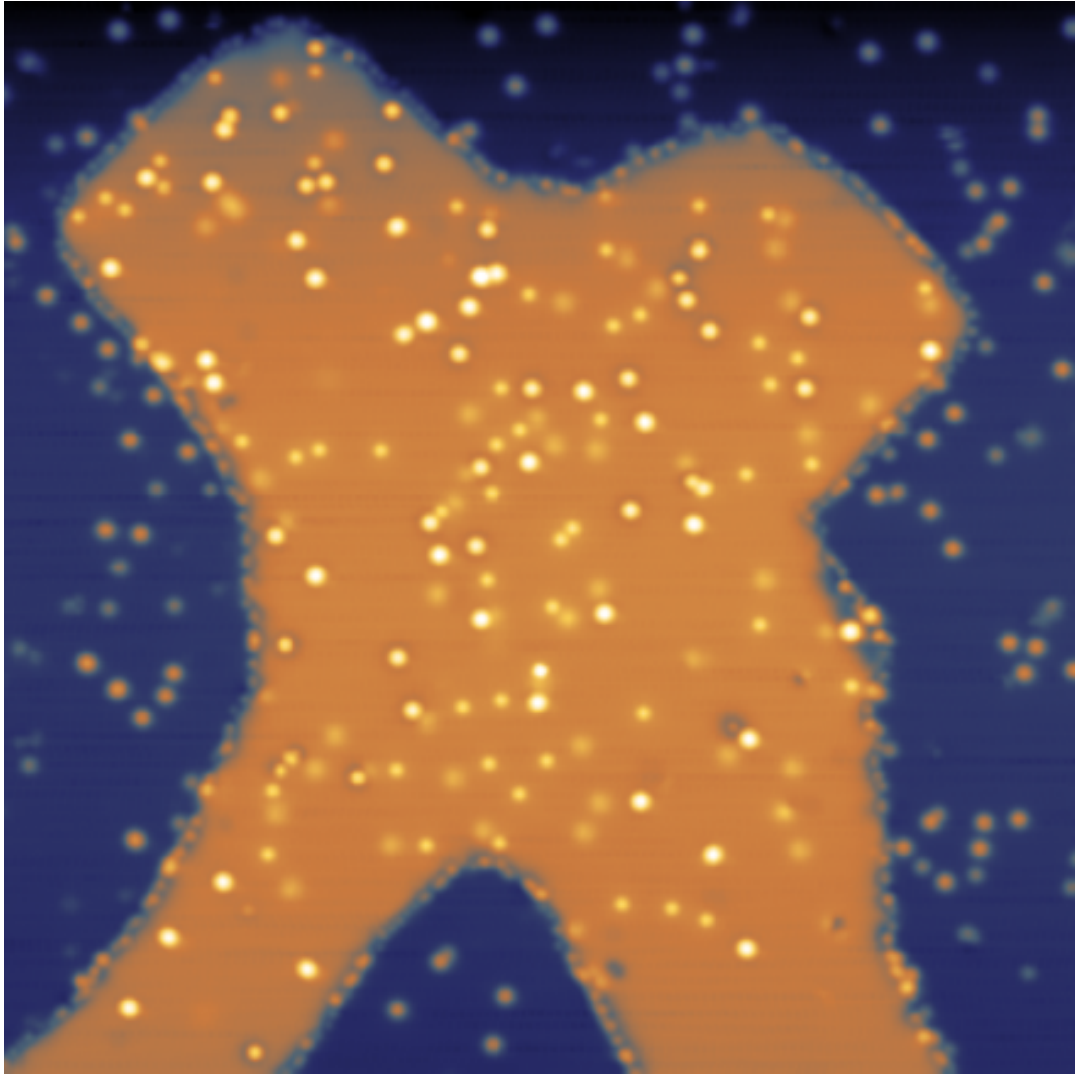
Figure 5.3: The blue area is the bare Ag(100) crystal. The orange area is an atomic double-layer of MgO on top of the Ag. Three species of atoms on top of the surface can be distinguished: 1. Fe atoms, 2. TiH molecules on top of O atoms of the MgO and 3. TiH molecules on top of bridge sites between two O atoms of the MgO.

microwave chopping input and lock-in current output can be eliminated by using the radial component of the lock-in current demodulation $R = \sqrt{X^2 + Y^2}$. By this method, even small changes in the current signal can be measured precisely.

5.4 Frequency Sweeps

For two different current setpoints, $50\,\mathrm{pA}$ and $175\,\mathrm{pA}$, and seven different magnetic fields respectively, the ESR lock-in signal was measured in depenency of frequency. The microwave amplitude is kept constant between frequency changes by compensating the previously measured transfer function. The ESR lock-in scheme is used to measure the ESR signal. The seven magnetic fields for $50\,\mathrm{pA}$ were $(2.125, 2.175, 2.25, 2.445, 2.54, 2.6, 3.323)\,\mathrm{T}$. For $175\,\mathrm{pA}$, the magnetic fields were set to $(2.05, 2.1, 2.175, 2.365, 2.465, 2.5525,$ $3.241)\,\mathrm{T}$. The reason for the difference is to compensate the stray field from the tip that can change with current setpoint. Only the frequency ranges where the ESR signal for the respective magnetic fields are expected were measured. The choice of the ranges is confirmed by seeing the ESR signal at the respective frequency range. The comparison of the peaks at two different current setpoints at the lowest magnetic field (see Fig. 5.4) shows that the peak width and height increase with setpoint. The width increase is expected and is probably a consequence of a decrease in T_2 and mechanical vibrations of the tip which cause fluctuations in the tip magnetic field [83, 84]. The corresponding measurement at highest frequency (see Fig. 5.5) demonstrates that we can perform ESR at frequencies close to $100\,\mathrm{GHz}$.

The magnetic field dependency of the lock-in current peak position shows that the peak is caused by ESR and not by a different effect. The frequency sweeps of all measured magnetic fields have a similar shape depending on their current setpoint (see Fig. 5.6). This shape can be modelled as a Fano function [5, 70] in order to extract the resonance frequency:

$$I_{\mathrm{LI}} = A \cdot \left(1 - \frac{(Q + \epsilon)^2}{1 + \epsilon^2}\right) + \delta \qquad (5.1)$$

where I_{LI} is the lock-in current, A the amplitude, δ the offset, Q the Fano factor and $\epsilon = \frac{\nu - \nu_0}{\gamma}$. ν is the frequency, ν_0 the resonance frequency and γ the linewidth. By plotting the extracted reso-

Figure 5.4: (a) Radial component of the lock-in current at a current setpoint of 50 pA and a magnetic field of $B = 2.125$ T (b) Radial component of the lock-in current at a current setpoint of 175 pA and a magnetic field of $B = 2.05$ T
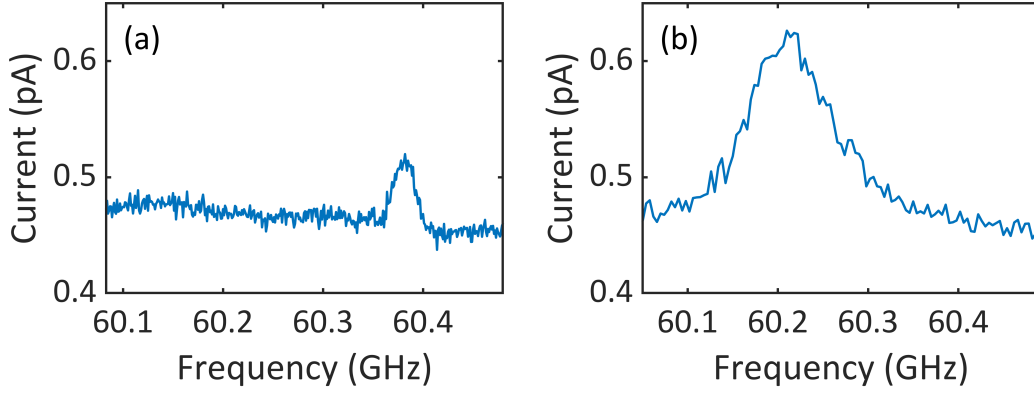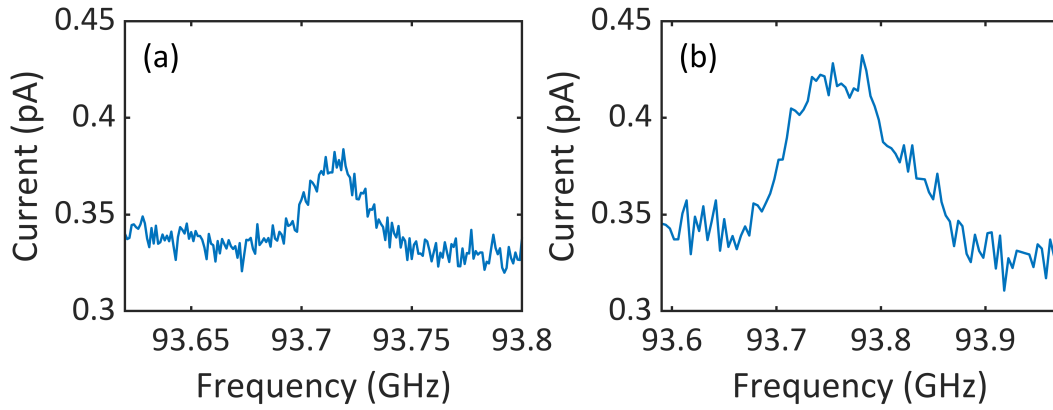

Figure 5.5: (a) Radial component of the lock-in current at a current setpoint of 50 pA and a magnetic field of $B = 3.323$ T (b) Radial component of the lock-in current at a current setpoint of 175 pA and a magnetic field of $B = 3.241$ T

nance frequency data in dependency of the magnetic field [7, 18], the g-factor can be extracted by a linear fit (see Fig. 5.7). For a setpoint of 50 pA, we obtain $g = 1.988$ and for 175 pA, we obtain $g = 2.005$. The values are in close agreement with each other. It can be seen that the Zeeman energy of the higher setpoint is shifted up compared to the lower setpoint. This may be attributed to the increased tip stray field due to the lower tip-sample distance at higher current setpoint. It may be speculated that the minor

g-factor deviation between the different setpoints is also influenced by this effect.
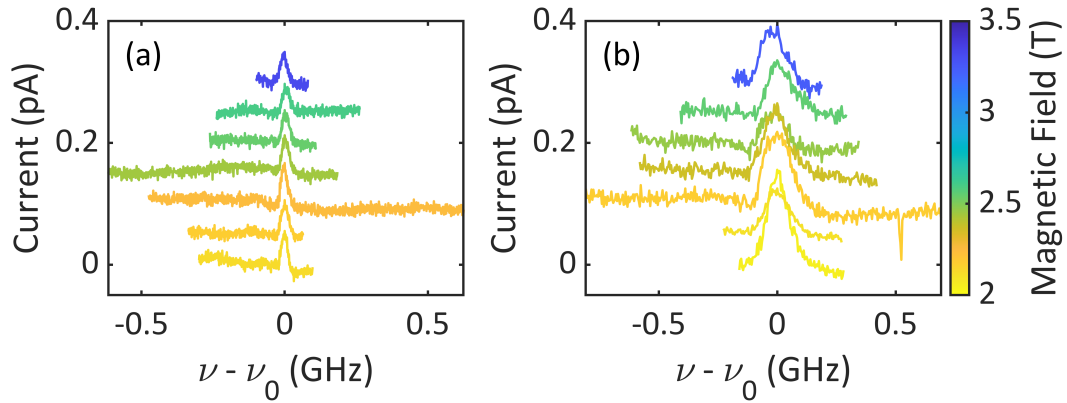

Figure 5.6: (a) Radial component of the lock-in currents at a current setpoint of 50 pA for different magnatic fields (b) Radial component of the lock-in currents at a current setpoint of 175 pA for different magnatic fields; For (a) and (b), the vertical offset of the lowest magnetic field sweep is normalized to zero. The baselines of the subsequent sweeps are offset by 50 fA to each other, respectively, for better visibility. Horizontally, the graphs are offset by the frequency of the respective peak maximum position ν_0.
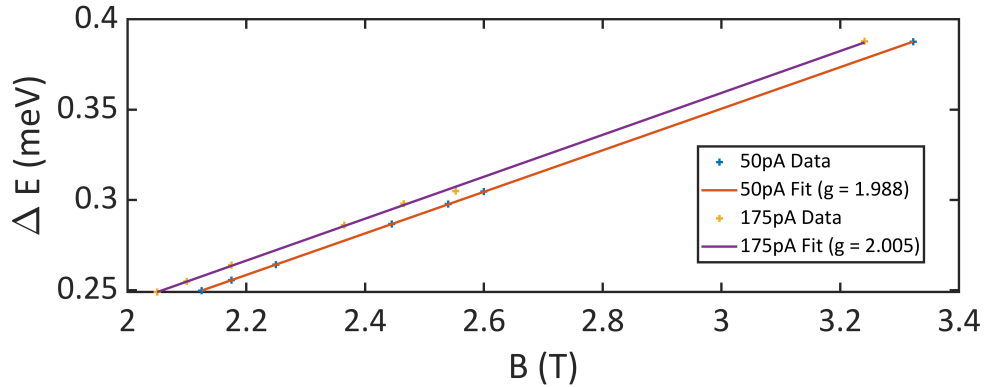

Figure 5.7: The data points are the Zeeman energies which are proportional to the resonance frequencies that have been extracted from measured peaks by using Fano line shape fits. These points are plotted in dependency of the applied magnetic field. *g*-factors of $g = 1.988$ for a setpoint of 50 pA and of $g = 2.005$ for a setpoint of 175 pA are determined from the slope of linear fits.

5.5 Magnetic Field Sweeps

Alternatively to the variation of the microwave frequency, the external magnetic field B can be varied while the microwave frequency remains constant. This measurement mode only requires knowledge of the transfer function for the single frequency point that is used. Thereby, this has the advantage that the measurement becomes unaffected by frequency dependent deviations of the transfer function which would cause deviations of the microwave amplitude. However, changing the magnetic field produces an eddy current which causes Joule heating. This also causes thermal drift which makes it more difficult to stay at the same atom. To compensate these effects, longer atom tracking times are implemented after magnetic field changes so that temperature and thermal expansion have time to relax. This makes the measurement longer compared to frequency sweeps.
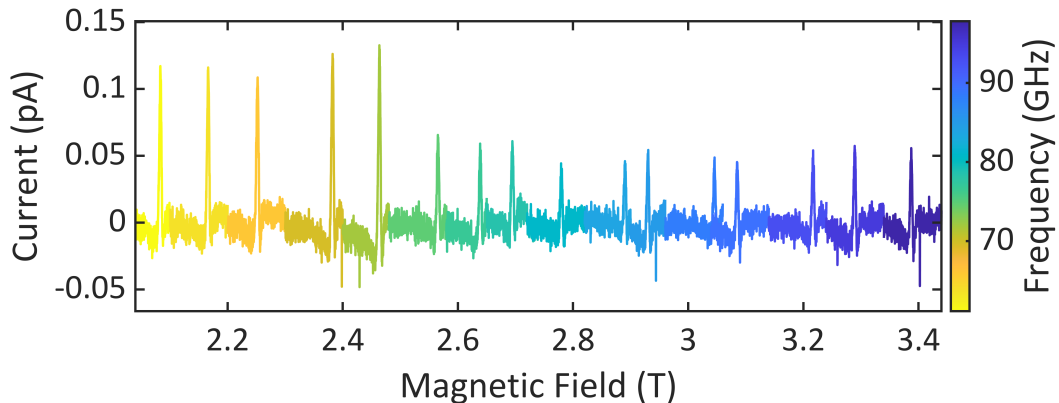
Figure 5.8: Radial component of the lock-in current in dependency of magnetic field for different frequencies: For better visibility, the vertical offsets of the different sweeps were equalized such that the baseline is at zero. The measurement frequencies are (61.14, 63.52, 65.96, 69.66, 71.95, 74.81, 76.86, 78.45, 80.82, 83.90, 85.02, 88.28, 89.40, 93.07, 95.08, 97.81) GHz.

Magnetic field sweeps were performed at 16 different frequencies at a current setpoint of 175 pA (see Fig. 5.8). The comparison between the line shapes of lowest and highest frequency yields similar results (see Fig. 5.9). As for the frequency sweeps, the line

shapes of all frequencies can again be fitted as a Fano shape by equation (5.1) to determine the resonance magnetic field B_0 by using $\epsilon = \frac{B-B_0}{\gamma}$.
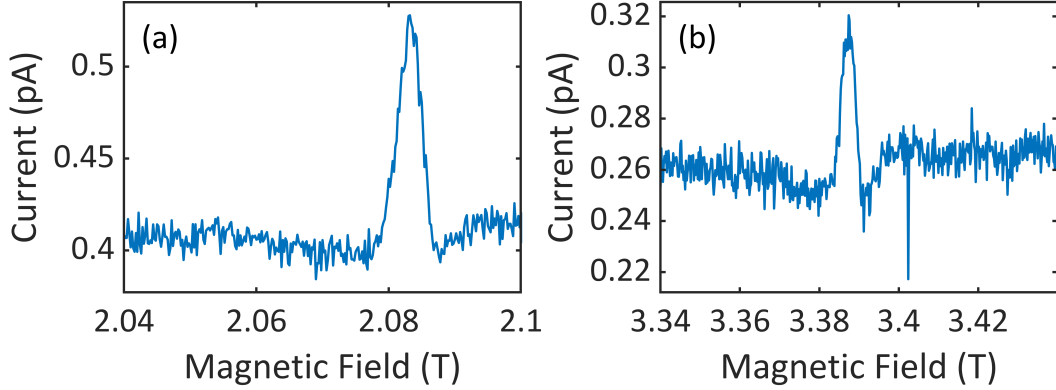
Figure 5.9: (a) Radial component of the lock-in current at a frequency of 61.14 GHz (b) Radial component of the lock-in current at a frequency of 97.81 GHz

The plot of the extracted resonance magnetic fields and Zeeman energies shows that the points lie on a straight line (see Fig. 5.10). A linear fit yields a g-factor of 2.008. This is similar to the g-factors $g = 1.988$ at 50 pA setpoint and $g = 2.005$ for 175 pA setpoint for the case of frequency sweeps. This shows that both methods, frequency sweeps and magnetic field sweeps, are accurate. The g-factor for magnetic field sweeps is closer to the frequency sweep value at 175 pA than at 50 pA. The magnetic field sweeps have also been carried out at a setpoint of 175 pA. This points further to the setpoint dependent tip stray field as an explanation for the minor deviation.

5.6 Conclusion

In conclusion, we may say that both, the frequency dependent and the magnetic field dependent ESR-STM measurement mode, have been demonstrated successfully. The similar values for the g-factors confirm that both methods are highly accurate and re-
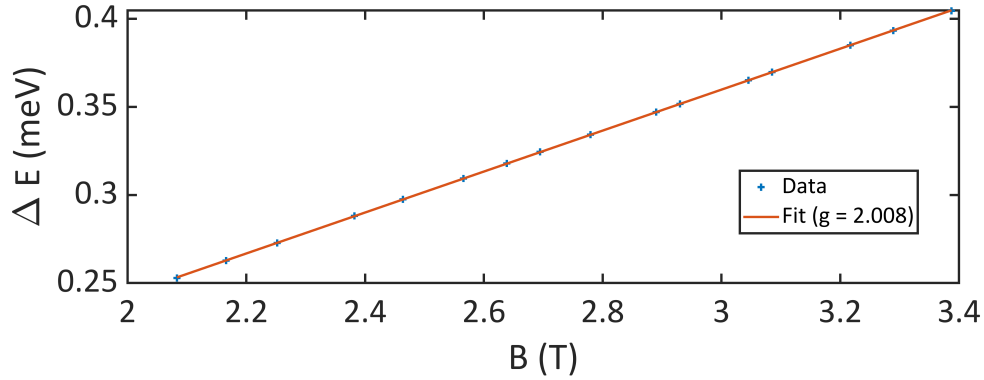
Figure 5.10: The data points are the resonance magnetic fields that have been extracted from measured peaks by using Fano line shape fits. The Zeeman energy is proportional to the applied frequency. A g-factor of $g = 2.008$ is determined from the slope of a linear fit.

producible. The results also validate the accuracy of our improved transfer function measurement schemes.

The extension of the frequency range up to $100\,\mathrm{GHz}$ opens up new possibilities for the study of single atom spin systems and nanostructures and their intrinsic dynamics. With frequencies above the Zeeman splitting, multiplet transitions can be observed for example. Furthermore, due to the increased frequency, the Zeeman energy becomes the dominating energy rather than the thermal energy.

6 Multiband Josephson Effect in Pb

6.1 Past Studies on Pb

The content of this chapter will be published in our paper [78].

Microwave radiation is not the only reason that can cause an apparent splitting of a superconductor's coherence peaks. The peaks can also be split inherently if the superconductor has multiple superconducting bands. This is the case for Pb. Pb is a type I superconductor with $T_C = 7.19\,\text{K}$ [79] and large spin-orbit coupling [50]. When a double structure in the tunneling current has first been observed [9, 48, 64, 77], it has originally been attributed to energy gap anisotropy due to the phonon density of states [8]. Later theoretical investigations revealed that anisotropy is actually not the reason for the double structure and instead identified the effect as two-band superconductivity from two sheets of the Fermi surface [23]. STM studies have confirmed this effect [62, 66].

6.2 Experimental Methods

A Pb tip is used on a Pb(110) surface. The sample was prepared *in situ* by multiple cycles of Ar sputtering and annealing. Sputtering was done at an Ar pressure of $5 \cdot 10^{-6}\,\text{mbar}$ to $6 \cdot 10^{-6}\,\text{mbar}$ for about one to two hours. Afterwards, for annealing, the sample was preheated in vacuum for about 6 min until it reached a temperature of 250 °C. This temperature was kept for a duration of approximately 30 min. The Pb tip was cut off Pb wire. It was
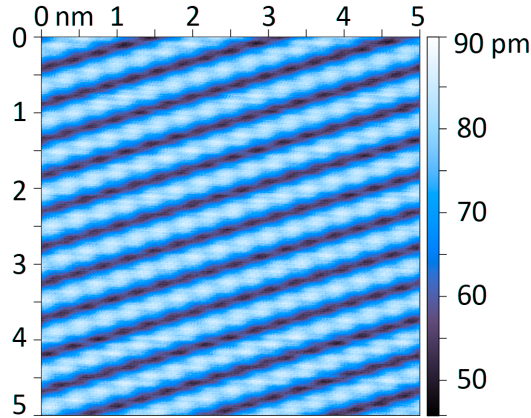
Figure 6.1: 5 nm by 5 nm Scan of the Pb(110) sample with atomic resolution

shaped by voltage pulses and ramming the tip into the Pb surface until topography and dI/dV spectroscopy gave no hint for impurities. The correct crystal orientation of the Pb(110) sample is confirmed by a scan with atomic resolution (see Fig. 6.1).

The base temperature during the measurement was 310 mK. The tunneling current I was measured with high resolution in dependency of bias voltage V. The derivative of the current with respect to bias voltage dI/dV was measured by a lock-in amplifier. Different normal state conductances G_N over multiple orders of magnitude were measured by varying the tip-sample distance (see Fig. 6.2 (a) and (c)). All measurements shown in the following were performed with the same microtip.

6.3 Data Preprocessing

The measured data has a bias voltage offset and a current offset. Those deviations are caused by the electronic devices involved in the measurement, not the actual tunneling process. Additionally, there are current dependent deviations due to cabling resistance, the voltage divider and the transimpedance amplifier. The cabling resistance $R_C = 158.3\,\Omega$ has been measured between bias voltage
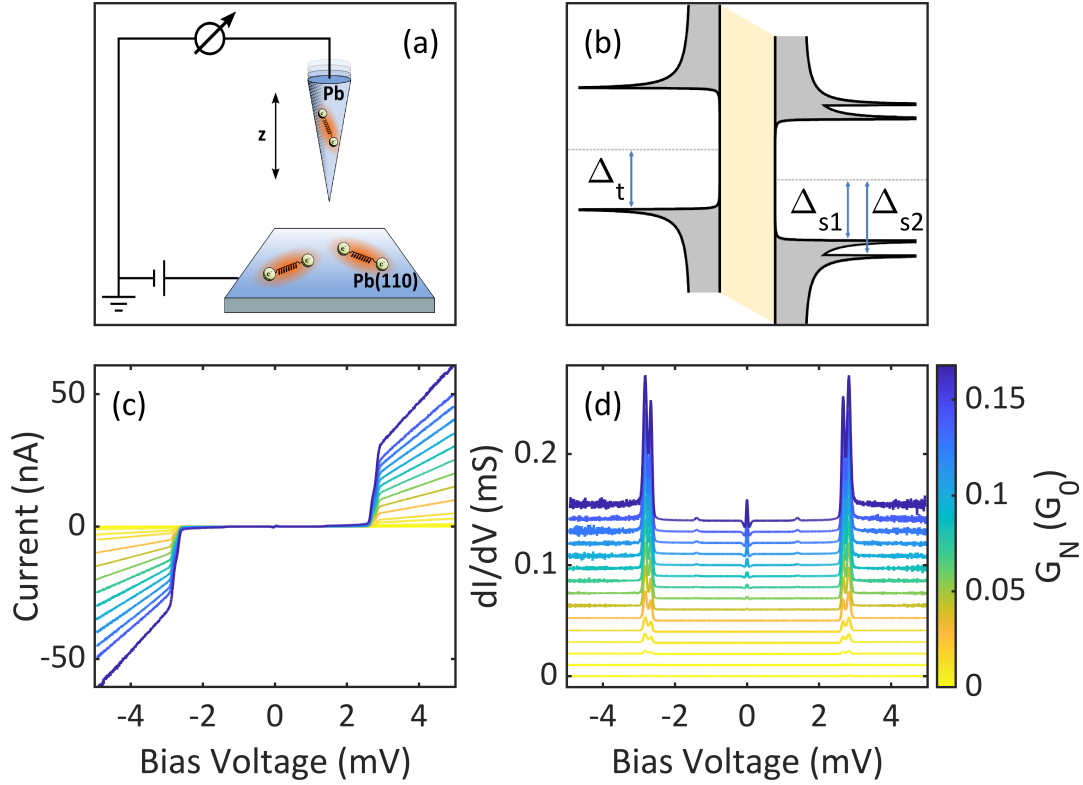
Figure 6.2: (a) Scheme of the STM setup with a Pb tip on a Pb(110) surface where the tip-sample distance is varied between the measurements (b) Densities of states in dependency of energy in the tip (left) and the sample (right) vertically offset by the bias voltage (c) Current in dependency of bias voltage for different normal state conductances G_N (d) dI/dV in dependency of bias voltage for different normal state conductances G_N: The two large outer peaks on each side are the coherence peaks. The multiband nature of Pb is apparent from their splitting. With increasing G_N, the Josephson effect emerges as an increasing peak at zero bias voltage. The dI/dV graphs for the different G_N are offset vertically with a distance of $10\,\mu S$ for better visibility. The color bar at the bottom right shows G_N of the graphs in (c) and (d) in units of the quantum of conductance G_0.

input and current output of the STM while the tip is rammed into the surface.

A voltage divider reduces the voltage from the bias voltage source before the STM input. This is necessary because the voltage source would not have a small enough voltage step size. A
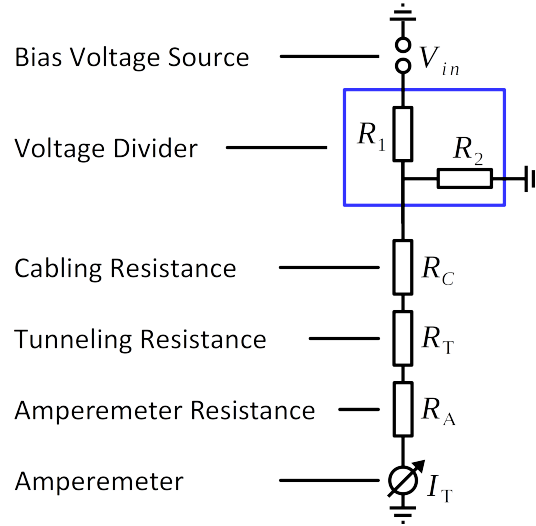
Figure 6.3: Circuit diagram of the STM with bias voltage source, voltage divider with internal resistances $R_1 = 9.9\,\mathrm{k\Omega}$ and $R_2 = 100\,\Omega$, cabling resistance $R_\mathrm{C} = 158.3\,\Omega$, tunneling resistance R_T and amperemeter resistance R_A

perfect voltage divider would divide the voltage by a constant factor. We divide by a factor of 100. However, this value is not accurate due to the underlying electronics: Internally, the voltage divider consists of two resistances $R_1 = 9.9\,\mathrm{k\Omega}$ and $R_2 = 100\,\Omega$ (see Fig. 6.3). If the voltage divider has an input voltage of V_in, the output voltage is approximately

$$V_\mathrm{out} = V_\mathrm{in} \cdot \frac{R_2}{R_1 + R_2} = V_\mathrm{in}/100. \tag{6.1}$$

This approximation is only valid for infinite STM resistance $R_\mathrm{STM} = R_\mathrm{T} + R_\mathrm{C} + R_\mathrm{A}$ where R_T is the tunneling resistance, R_C the cabling resistance and R_A the transimpedance amplifier internal resistance. The tunneling resistance is the most significant contribution to the STM resistance. In this experiment, we reduce the tunneling resistance by orders of magnitude to less than $100\,\mathrm{k\Omega}$ compared to the usual multiple $\mathrm{M\Omega}$ by reducing the tip sample distance. Therefore, the consideration of the current dependent

deviation is necessary for reaching high accuracy. The general voltage divider output voltage is

$$V_{\text{out}} = V_{\text{in}} \cdot \frac{R_2 || R_{\text{STM}}}{(R_1 + R_2) || R_{\text{STM}}} \tag{6.2}$$

where R_{STM} is determined by the tunneling current I_{T} by

$$R_{\text{STM}} = \frac{V_{\text{out}}}{I_{\text{T}}} \tag{6.3}$$

and the parallel circuit operation $||$ is defined by

$$R_2 || R_{\text{STM}} = \frac{R_2 \cdot R_{\text{STM}}}{R_2 + R_{\text{STM}}}. \tag{6.4}$$

Solving the two-dimensional equation system (6.2), (6.3) for R_{STM} yields

$$R_{\text{STM}} = \frac{V_{\text{in}}/I_{\text{T}} - R_1}{1 + \frac{R_1}{R_2}}. \tag{6.5}$$

The transimpedance amplifier transforms the tunneling current into a voltage that is measured. The gain is the factor to transform between tunneling current and measured voltage. We use the gains 10^8 V/A and 10^9 V/A depending on the tunneling resistance. The transimpedance amplifier internal resistance R_{A} depends on the gain. For gain 10^8 V/A, we use $R_{\text{A}} = R_{\text{A1}}$. For gain 10^9 V/A, we use $R_{\text{A}} = R_{\text{A2}}$.

The total voltage that arrives at the tunnel junction is

$$V_{\text{T}} = \frac{V_{\text{in}} - R_1 I_{\text{T}}}{1 + \frac{R_1}{R_2}} - (R_{\text{C}} + R_{\text{A}}) \cdot I_{\text{T}}. \tag{6.6}$$

The different resistances can be combined into one effective resistance $\frac{R_1}{1+\frac{R_1}{R_2}} + R_{\text{C}} + R_{\text{A}}$. The only unknown parameter R_{A} effectively also includes all other resistances that have not been considered yet that are in series with the tunnel junction and after the voltage divider. Additional resistances before the voltage divider are not considered because they would effectively change the known value for R_1.

Different ways to compensate the bias voltage offset were tried. The best way has been found to be based on the coherence peaks: There are four coherence peaks for each $\mathrm{d}I/\mathrm{d}V$ curve in dependency of bias voltage, two at positive bias voltage and two at negative bias voltage. They are the four largest peaks in each of the $\mathrm{d}I/\mathrm{d}V$ curves (see Fig. 6.2 (d)). The bias voltage offset determination uses the property that the bias voltage positions of the coherence peaks must be symmetric around zero bias voltage. The reason for this is that the coherence peaks at positive and negative bias voltage are determined by the same gap parameters as explained in section 6.4.

The deviations described in this section are compensated by the following procedure: The four coherence peak positions of each normal state conductance are determined by Lorentzian fits of the $\mathrm{d}I/\mathrm{d}V$ raw data. The resulting bias voltage offset is compensated for each normal state conductance individualy. The current must be antisymmetric in bias voltage. The current offset is corrected for each normal state conductance by subtracting the respective current mean value. Averaging the bias voltage offset or current offset over the different normal state conductances would not make sense because the offsets can change during the different measurements.

The remaining deviation is a scale stretching of the bias voltage that arrives at the tunnel junction compared to the bias voltage input that is described by equation (6.6). Its only unknown parameters are (R_{A1}, R_{A2}). Due to the current dependency of equation (6.6), the bias voltage scales are stretched differently for the different normal state conductances. Therefore, the coherence peaks appear to be at slightly different bias voltage positions. The two-dimensional vector (R_{A1}, R_{A2}) is fitted by a minimization of the coherence peak position standard deviation between the different normal state conductances based on equation (6.6). To improve efficiency, this fit is first performed based on coherence peak maximum positions. The resulting values for (R_{A1}, R_{A2})

are used as initial guess to fit it again more accurately based on Lorentzian fits of the coherence peaks. The resulting values $(R_{A1}, R_{A2}) = (981.6\,\Omega, 10424.0\,\Omega)$ are used to calculate the corrected bias voltage with equation (6.6). Another bias voltage offset correction based on Lorentzian fits of the coherence peaks is applied.

The dI/dV data has an arbitrary scaling factor due to the lock-in preamplifier by which it has been measured. After the preprocessing described so far, this scaling factor is determined by minimizing the deviation between the Savitzky-Golay [67] filtered dI/dV data and the numerical derivative of the Savitzky-Golay filtered current data. The dI/dV data is then multiplied by this scaling factor to obtain a differential conductance in Siemens. The Savitzky-Golay filter [67] filters out noise in the data and is only used to reduce deviations of the scaling factor. It is not applied on the data for the further analysis.

The data after preprocessing is shown in Fig. 6.2 (c) and (d). The total bias voltage correction changes the bias voltage maxima by $0.3\,\%$ for the minimum current setpoint and by $1.8\,\%$ for the maximum current setpoint in relation to the raw data. Even though this deviation may seem small, it is still important. Firstly, it is well on the order of our accuracy. Secondly, it can easily have superlinear effects on the results. For example, symmetry violations due to incorrect offset corrections, different offsets between the different measurement sweeps or incorrect current dependent offset corrections can cause fits to fail. The current offset is typically around $-6.3\,\mathrm{pA}$ for gain $10^8\,\mathrm{V/A}$ and around $-0.50\,\mathrm{pA}$ for gain $10^9\,\mathrm{V/A}$.

6.4 Gap Parameter Determination

The most important parameters for the analysis are the gap parameters Δ_t of the tip and $\Delta_\mathrm{s1}, \Delta_\mathrm{s2}$ of the two bands of the sample. In contrast to the sample, the tip is not a single crystal and can

therefore be treated with one mixed band. For the sample, it is necessary to consider both bands.

It can easily be seen in Fig. 6.2 (b) that an overlap of tip and sample density of states creates a large current only if the bias voltage shift between tip and sample exceeds the sum of tip and sample gap parameter, $eV \geq \Delta_\mathrm{t} + \Delta_{\mathrm{s}j}$ for each of the two bands $j \in \{1, 2\}$, respectively.

In the $\mathrm{d}I/\mathrm{d}V$ graph, different peaks become apparent (see Fig. 6.2 (d)): The two outer peaks on each side are the coherence peaks at $\pm\left(\Delta_\mathrm{t} + \Delta_{\mathrm{s}j}\right)/e$. The peak at zero bias voltage originates from the Josephson effect. The small peaks in between are overlapping peaks at $\pm\Delta_\mathrm{t}/e$, $\pm\Delta_{\mathrm{s}1}/e$ and $\pm\Delta_{\mathrm{s}2}/e$ from first order Andreev reflections.
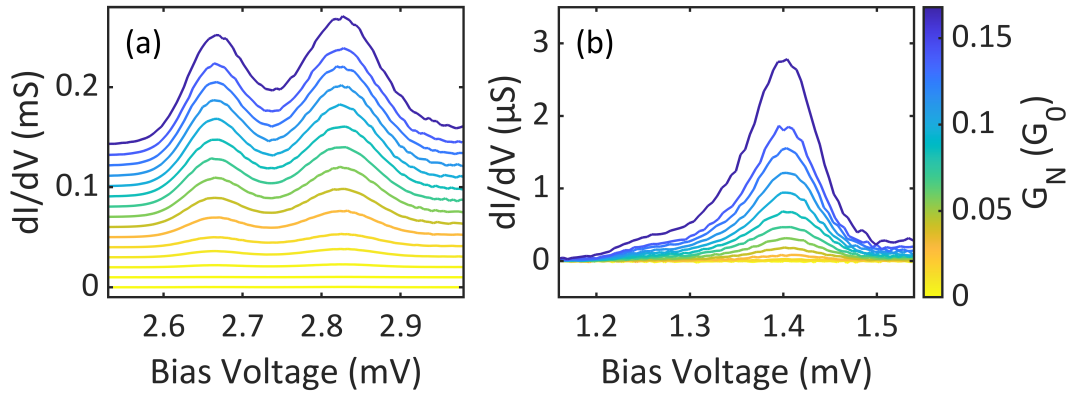
Figure 6.4: (a) Zoom in to $\mathrm{d}I/\mathrm{d}V$ of the two coherence peaks at positive bias voltage in dependency of bias voltage for different normal state conductances G_N: The graphs for the different G_N are offset vertically with a distance of $10\,\mathrm{\mu S}$ for better visibility. (b) Zoom in to $\mathrm{d}I/\mathrm{d}V$ of the first order Andreev reflection peaks at positive bias voltage in dependency of bias voltage for different normal state conductances G_N without offset: The feature is a superposition of three peaks at $eV = \Delta_{\mathrm{t,s1,s2}}$, respectively. While there is clearly a smaller side peak at lower bias voltage $V = \Delta_{\mathrm{s}1}/e$, the positions of the two peaks at $V = \Delta_{\mathrm{t,s2}}/e$ are hard to distinguish. The color bar on the right shows G_N of the graphs in (a) and (b) in units of the quantum of conductance G_0.

In order to determine the respective parameters $\Delta_{\mathrm{t,s1,s2}}$, we need more information besides the two coherence peak positions (see

Fig. 6.4 (a)). One possibility is to extract that directly from the positions of the first order Andreev reflection peaks located at $eV = \Delta_{t,s1,s2}$, but since they are broadened and quite close to each other largely overlapping, this method is ambiguous (see Fig. 6.4 (b)). Another possibility is to estimate the dependence of Δ_t on $\Delta_{s1,s2}$ theoretically. According to the McMillan formula [51], the tip gap is a mix of the gap from two bulk superconducting bands

$$\Delta_t = \frac{\Gamma_2 \Delta_{s1} + \Gamma_1 \Delta_{s2}}{\Gamma_1 + \Gamma_2}, \tag{6.7}$$

where Γ_j are hopping parameters between the two bands satisfying $\Gamma_1/\Gamma_2 = n_2/n_1$ with $n_{1,2}$ being the normal electronic density of state of bulk Pb near the Fermi energy. This assumes interband hopping from band 1 to band 2 and vice versa. Due to the polycrystalline tip, there is scattering and a strong coupling between the tip bands. The approximation of using one effective tip gap parameter is valid for large Γ_j.

From first principle band structure calculations done by Haonan Huang, we determine that $n_2/n_1 = 2.4$ with band 1 accommodating a nearly spherical Fermi surface surrounding the Γ point hosting a smaller superconducting gap ($\Delta_1 < \Delta_2$). Plugging equation (6.7) in the two coherence peak positions $\pm (\Delta_t + \Delta_{s1})/e$ and $\pm (\Delta_t + \Delta_{s2})/e$, we obtain values of $\Delta_t = 1.3892\,\mathrm{meV}, \Delta_{s1} = 1.2772\,\mathrm{meV}, \Delta_{s2} = 1.4360\,\mathrm{meV}$ which we use in the following analysis. The resulting predictions of the positions of the multiple Andreev reflections are consistent with the experimental observations which validates the above theoretical treatment (see Fig. 6.4 (b)).

6.5 Josephson and Quasiparticle Fits

First of all, we fit the normal state conductance G_N to $\mathrm{d}I/\mathrm{d}V$ for the different tip-sample distances to get an initial guess for the values of G_N. We apply the Ambegaokar-Baratoff formula (2.17)

[3] generalized for multiple bands to obtain the critical current I_{C} in dependency of G_{N},

$$I_{\mathrm{C}} = \sum_{c=1}^{n} \frac{\tau_c G_0}{e} \Delta_1^{(j_c)} \cdot K \left(1 - \left(\frac{\Delta_1^{(j_c)}}{\Delta_2^{(j_c)}} \right)^2 \right), \qquad (6.8)$$

where $\boldsymbol{\tau}$ is the transmission vector or mesoscopic PIN-code, $n = \dim(\boldsymbol{\tau})$ the number of transmission channels, $G_0 = 2e^2/h$ the quantum of conductance, $\Delta_1^{(j_c)} = \min\left(\Delta_{\mathrm{t}}, \Delta_{\mathrm{s}j_c}\right)$ the smaller of the two gap parameters of tip and sample, $\Delta_2^{(j_c)} = \max\left(\Delta_{\mathrm{t}}, \Delta_{\mathrm{s}j_c}\right)$ the larger of the two gap parameters and K the complete elliptic integral of the first kind. Each component τ_c of the PIN-code $\boldsymbol{\tau}$ is associated to a transmission channel c from one of the two bands with index j_c. The total transmission is the sum of all components of $\boldsymbol{\tau}$. As the linear dependency of I_{C} on G_{N} only holds in the dynamical Coulomb blockade regime where the Josephson energy E_{J} is small compared to the Coulomb charging energy [40], this yields critical current values that are only accurate for small G_{N}.

We use these values for small G_{N} only as a starting point for our calculation as described in the following. This calculation will yield more reliable values for the critical current for all G_{N} from the first order Fourier calculation described later. We use these more accurate values to repeat the calculation from here similar to a self-consistent approach.

We use $P(E)$ theory [16, 39] to describe the Josephson current in dependency of the local electromagnetic environment,

$$I(V) = \frac{\pi e E_{\mathrm{J}}^2}{\hbar} \left(P(2eV) - P(-2eV) \right), \qquad (6.9)$$

where E_{J} is the Josephson energy and P describes the probability of the tunneling Cooper pair to exchange a photon of energy E with the environment. E_{J} determines the critical current I_{C}. The environment enters the calculation as an electromagnetic impedance described by a capacitance C_{J} and a transmission line model (see equations (2.23) and (2.24) in section 2.4). Addition-

ally, we consider temperature and external noise as well as lock-in broadening.

Due to the way our fit function depends on E_J and the environmental DC resistance, only one of them can be reliably extracted from the fit and the other one must be set as a constant. From the above calculation of I_C for low G_N and the relation between I_C and E_J, we know E_J for low G_N. This allows us to fit the impedance parameters at a reference normal state conductance of $G_N = 0.014 \, G_0$ (see Fig. 6.5 (a)). This is the lowest G_N for which we can measure a low-noise Josephson current. At lower G_N, the signal-to-noise ratio necessarily becomes worse because the reduction of noise with G_N is slower than the approximately quadratic decrease of the Josephson current. At higher G_N, the Ambegaokar-Baratoff formula becomes inaccurate. We assume that the impedance parameters of the local environment that are extracted at the reference normal state conductance are independent of G_N.
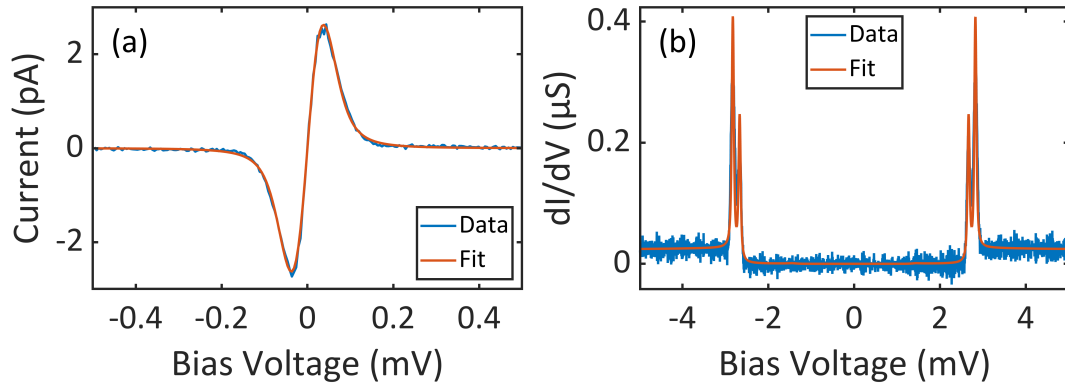
Figure 6.5: (a) Fit of the Josephson current by $P(E)$ theory at the reference normal state conductance $G_N = 0.014 \, G_0$ to obtain the impedance parameters of the local electromagnetic environment (b) Quasiparticle Fit of dI/dV at low $G_N = 0.3 \cdot 10^{-3} \, G_0$

We use these extracted impedance parameters and gap parameters to fit the Dynes broadening η to dI/dV (see Fig. 6.5 (b)). This is done at lowest G_N in order to not be disturbed by Josephson effect or Andreev reflections which only become relevant at higher G_N. In contrast to the Josephson current fit where dif-

ferent broadening mechanisms were distinguished, in this $\mathrm{d}I/\mathrm{d}V$ fit, we use the approximation of considering $P(E)$, external noise and lock-in broadening in η so that we can use this η as a starting value for a calculation of multiple Andreev reflections where a direct consideration of $P(E)$ theory would not be feasible. As we cannot reasonably distinguish different broadenings at tip and sample, we assume that η is the same for both.
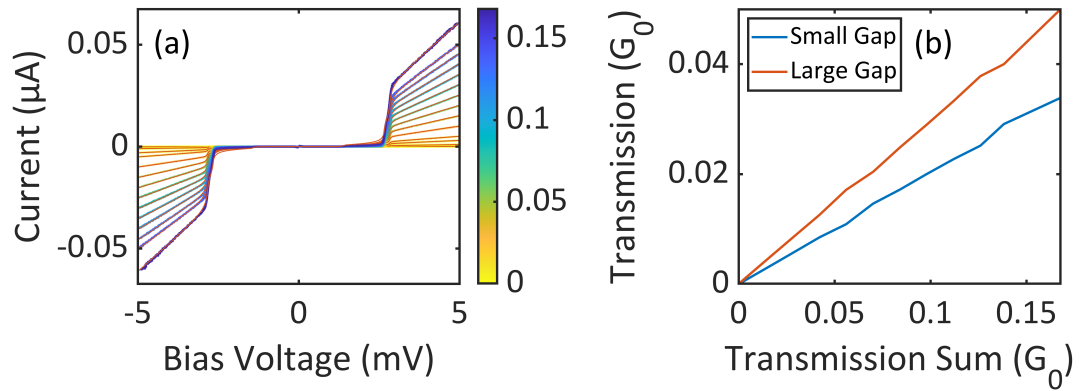
6.6 Multichannel Calculation

Figure 6.6: (a) Multichannel fits of the current for different G_N: The graphs of the measured current are shown in a color that represents their G_N on the shown color scale in units of G_0. The respective multichannel fits are plotted on top in orange. (b) Transmissions through each of the doubly degenerate channels $\tau_1 = \tau_2$ for the small gap and $\tau_3 = \tau_4$ for the large gap in dependency of G_N. The total transmissions for each band are obtained by multiplying the depicted numbers by 2 due to the degeneracy.

In order to obtain the PIN-code $\boldsymbol{\tau}$, we use the gap parameters and η to do a multichannel fit to the currents of the different G_N (see Fig. 6.6 (a)). This fit describes multiple Andreev reflections by the Andreev matrix [12, 13]. For this calculation, a certain configuration of conduction channels has to be assumed. The channel configuration is defined by a number of channels, a vector that assigns a band index to every channel and the degeneracy of the

channels. As it is always possible to assume additional channels that do not contribute significantly, the simplest channel configuration that yields good fit results is to be found. This is a doubly degenerate channel through each of the two bands, resulting in four conduction channels in total with $\tau_1 = \tau_2$ for the small gap and $\tau_3 = \tau_4$ for the large gap. Leaving out only one of these channels worsens the fit results dramatically. The fit result is the PIN-code $\boldsymbol{\tau}$. Figure 6.6 (b) shows τ_1 and τ_3 in dependency of G_{N}. Repeating this calculation with different values for η achieves the best fits at $\eta = 9.607\,\mathrm{\mu eV}$ which is lower than the approximate starting value from the $\mathrm{d}I/\mathrm{d}V$ fit. This approach eliminates the influence of potential broadening deviations in the $\mathrm{d}I/\mathrm{d}V$ fit. A problem here is that, while we assume the same η for everything, the current at the coherence peaks has a smaller broadening than at the Andreev reflections. We may speculate that this is because multiple Andreev reflections, in contrast to tunneling quasiparticles, undergo broadening mechanisms multiple times. Again, this is limited by the current unavailability of considering $P(E)$ theory and multiple Andreev reflections at the same time.

We use the resulting PIN-code in dependency of G_{N} to calculate the Fourier components of the energy-phase relation [71]. In order to do that, we use a generalization of equation (2.20) for multiple conduction channels which can be from different bands. c denotes the conduction channel index and m the number of Cooper pairs being transferred.

$$E(\phi) = \sum_{c=1}^{n} \sum_{m=-\infty}^{\infty} E_m^{(c)} \mathrm{e}^{im\phi} \tag{6.10}$$

The generalized Fourier components $E_m^{(c)}$ depend on c and m and the transmission τ_c depends on c as well:

$$E_m^{(c)} = -\Delta \sum_{k=|m|}^{\infty} \binom{1/2}{k} \binom{2k}{k+m} (-1)^{m+k} \left(\tau_c/4\right)^k. \tag{6.11}$$

Figure 6.7 (a) shows that the Fourier components of the two bands for first order $m = 1$ are very close to the respective $E_{\mathrm{J}}/2$. We
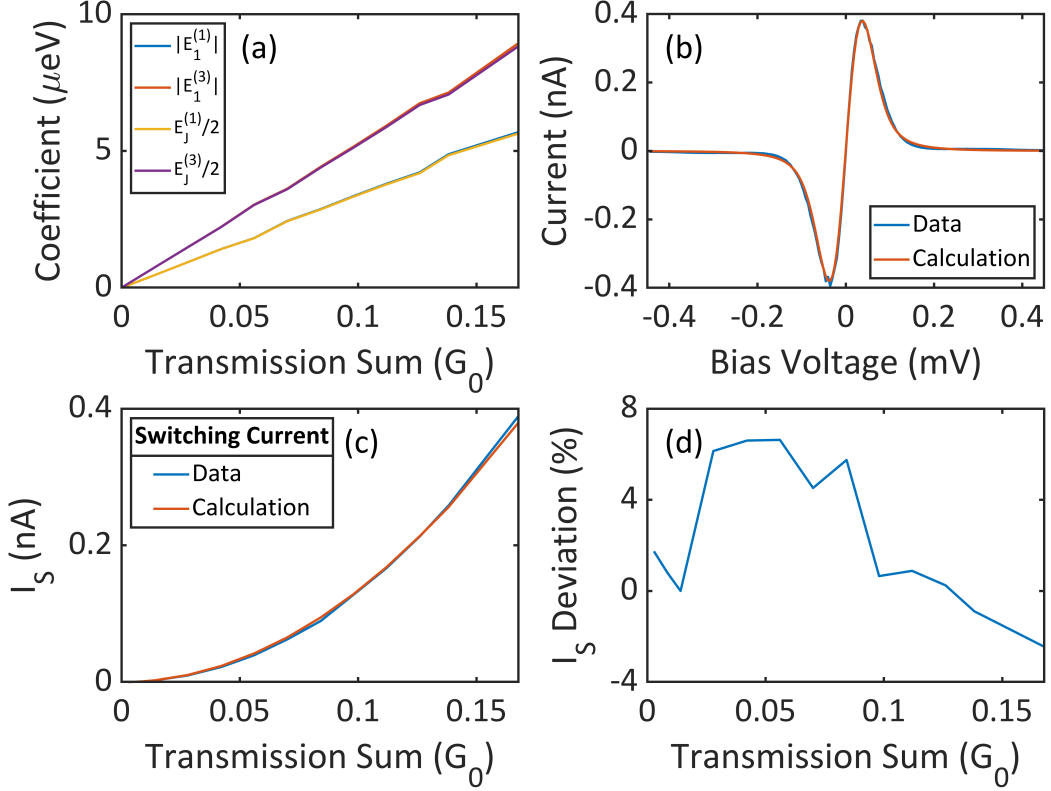
Figure 6.7: (a) Fourier components of first order compared to $E_{\mathrm{J}}/2$ (b) Comparison between Josephson current measurement and Fourier component calculation (c) Comparison between switching current measurement and Fourier component calculation (d) Relative Deviation of the Fourier component calculation of the switching current from the measurement

use the Fourier components up to order $m = 4$ in dependency of G_{N} to directly calculate the full bias voltage dependent Josephson current (see Fig. 6.7 (b)) using the following formula [71] that has been generalized to multiple channels

$$I(V) = \frac{2\pi}{\hbar} \sum_{m=1}^{\infty} \left| \sum_{c=1}^{n} E_m^{(c)} \right|^2 (2me) \left(P_m(2meV) - P_m(-2meV) \right).$$

(6.12)

The switching current I_{S} is the maximum of the bias voltage dependent Josephson current (see Fig. 6.7 (b)). Due to the symmetry, it is equivalent to the negative minimum. To evaluate the quality of our calculation, we can compare I_{S} in dependency of G_{N} from our

calculation to the data (see Fig. 6.7 (c)). The resulting average of the absolute value of the relative deviation of the I_S calculation from the data is only $2.87\,\%$ (see Fig. 6.7 (d)). This is a small deviation considering that the measurement ranges over multiple orders of magnitude in G_N.

Throughout our calculation, we can treat the two bands independently of each other and model the current just as a sum through both bands.

Our analysis shows how we can understand different tunneling processes in a multiband Josephson junction. It enables the extraction of previously unaccessible microscopic properties of the system. Values that have previously often been combined to single effective values can now be separated into their multiple contributions: We can characterize how the current is distributed over multiple conduction channels through multiple bands. We can distinguish the different gap parameters of the tip and both sample bands. We can disentangle different broadening mechanisms such as temperature, $P(E)$ theory, lock-in broadening and external noise.

The agreement between theory and experiment over multiple orders of magnitude in normal state conductance exhibits a high level of accuracy. The consideration of $P(E)$ theory, multiple Andreev reflections and the above separations of contributions brings the experimental confirmation of theory to a deeper level than before. This will allow for the understanding of even more complicated superconductor configurations and their applications in the future.

7 Summary of Results and Outlook

7.1 High Frequency Signal

By building an external antenna into an STM, the transmission of a high frequency signal to the tunnel junction was demonstrated successfully. A range of different methods for compensating the transfer function were implemented. By fitting the full Tien-Gordon equation [20, 65, 75], the transfer function can be determined reliably based on nonlinearities in the current-voltage curve which exist for example in superconductors. The efficient peak height method is an innovative approach to greatly increase measurement efficiency. The implementation of feedback averaging and an error correction protocol allow for a measurement cycle of ever increasing accuracy. The lock-in rectification method [57] [70] was improved by fitting the full Tien-Gordon equation, using smooth spline interpolation and combining it with feedback averaging as well as the error correction protocol. On the whole, the efficiency and accuracy of transfer function compensation has been improved significantly compared to the existing methods.

Our approach can be used by other scientific groups to augment a conventional STM by a high frequency antenna. Depending on the studied system's nonlinearity of the current-voltage characteristic, one of the improved transfer function measurement methods can be used. The transfer function compensation allows for keeping the microwave amplitude constant over a wide frequency range.

7.2 Electron Spin Resonance

ESR-STM has been demonstrated in a frequency range from 60 GHz up to 100 GHz. The g-factors of the system have been determined by sweeping the frequency as well as the magnetic field. The results of the different methods are in good agreement with each other.

This demonstration opens up new opportunities of exploration for ESR-STM in general. The increased Zeeman energy compared to previous implementations reduces the need for low temperatures to reach higher accuracies. Additionally, spin transitions can be observed in a wider range of systems.

Our approach can serve as a model for extending the ESR-STM technique to further STMs. In the future, spin dynamics [58, 88] as well as spin interactions [11, 82] can be studied further and in higher frequency ranges than before. The deeper understanding of the behavior of single spin systems is useful for quantum computation. Also, ESR measurements at molecules can be performed in dependency of space. This can identify spin centers in molecules which may be important for medical purposes.

7.3 Multiband Josephson Effect

The exploration of the multiband Josephson effect allows for the extraction of the following important microscopic parameters which is only possible by combining highly precise measurements with $P(E)$ theory [16, 39] and the theory of multiple Andreev reflections [12, 13]: The contribution of different conduction channels over multiple bands can be disentangled. The effect of broadening mechanisms such as thermal broadening, $P(E)$ broadening and external noise can be separated. The impedance parameters of the local electromagnetic environment can be determined. The precise agreement of the switching currents between fit and data

shows that the model works well over multiple orders of magnitude in normal state conductance.

This deep understanding of the multiband Josephson effect is relevant for general multiband superconductivity. Applications for superconductors will require a broader range of available superconducting materials including high T_C superconductors. Many of those will have multiple superconducting bands. The insight in the simple two-band superconductor Pb can help to understand the mechanisms in more complicated multiband superconductors. Our measurement and analysis methods can be used as a starting point to investigate those other superconductors. Furthermore, many quantum technologies depend on the Josephson effect. Specifically, the Josephson effect is the basis for the qubit architecture of all competitive quantum computer implementations. The presented insights in the multiband Josephson effect are thus of high importance for further research.

8 Acknowledgments

This work has only been possible thanks to the support of many people. I would like to say thank you to all those who helped me to conduct this research.

First of all, I am very grateful to Priv.-Doz. Dr. Christian R. Ast for accepting me as a PhD student at his ERC project at the Max-Planck Institute for Solid State Research and for being my thesis supervisor. I learned a lot from the many tips that he gave me and enjoyed the scientific discussion with him.

I am very thankful to Dr. Robert Drost for supporting me in every regard. His advice helped me to overcome many problems that appeared during the project.

Conducting experiments as challenging as ESR-STM requires working in a team. I thank Piotr Kot for working together at the experiment.

I thank Prof. Dr. Klaus Kern for accepting me at his department. I would also like to thank all members of the Kern department who have always been very helpful if there were things to fix at the lab, especially Janis Siebrecht and Haonan Huang.

I thank especially Dr. Thomas Keller who was the external adviser of my thesis committee. His counseling helped me a lot.

I am very grateful to Prof. Dr. Sebastian Loth for being a member of my examination board. Also, I am very grateful to Prof. Dr. Maria Daghofer for being the chairman of my examination board.

Finally, I would like to thank a lot my mother, father, brother, the rest of my family and my friends for the great support during the time of this work.

9 References

[1] M. S. Altman, "Evidence of a Pb(110) (2×2) reconstruction", Surface Science **344**, 65 (1995).

[2] M. S. Altman, E. Bauer, "The reconstructions of the Pb(110) surface studied by low energy electron microscopy", Surface Science **344**, 51 (1995).

[3] V. Ambegaokar, A. Baratoff, "Tunneling Between Superconductors", Phys. Rev. Lett. **10**, 486 (1963).

[4] C. R. Ast et al., "Sensing the quantum limit in scanning tunnelling spectroscopy", Nature Communications **7**, 13009 (2016).

[5] Y. Bae et al., "Enhanced quantum coherence in exchange coupled spins via singlet-triplet transitions", Sci. Adv. **4**, eaau4159 (2018).

[6] S. V. Bakurskiy, A. A. Golubov, M. Y. Kupriyanov, "Basic Properties of the Josephson Effect", in *Fundamentals and Frontiers of the Josephson Effect*, edited by F. Tafuri (Springer International Publishing, Cham, 2019), pp. 81–116.

[7] S. Baumann et al., "Electron paramagnetic resonance of individual atoms on a surface", Science **350**, 417 (2015).

[8] A. J. Bennett, "Theory of the Anisotropic Energy Gap in Superconducting Lead", Phys. Rev. **140**, A1902 (1965).

[9] B. L. Blackford, R. H. March, "Tunneling Investigation of Energy-Gap Anisotropy in Superconducting Bulk Pb", Phys. Rev. **186**, 397 (1969).

[10] C. J. Chen, "Introduction to Scanning Tunneling Microscopy" (Oxford Science Publications, 2015).

[11] T. Choi et al., "Atomic-scale sensing of the magnetic dipolar field from single atoms", Nature Nanotech. **12**, 420 (2017).

[12] J. C. Cuevas, W. Belzig, "Full Counting Statistics of Multiple Andreev Reflections", Phys. Rev. Lett. **91**, 187001 (2003).

[13] J. C. Cuevas, A. Martín-Rodero, A. Levy Yeyati, "Hamiltonian approach to the transport properties of superconducting quantum point contacts", Phys. Rev. B **54**, 7366 (1996).

[14] F. Delgado, J. Fernández-Rossier, "Spin decoherence of magnetic atoms on surfaces", Progress in Surface Science **92**, 40 (2017).

[15]M. L. Della Rocca et al., "Measurement of the Current-Phase Relation of Superconducting Atomic Contacts", Phys. Rev. Lett. **99**, 127005 (2007).

[16]M. H. Devoret et al., "Effect of the electromagnetic environment on the Coulomb blockade in ultrasmall tunnel junctions", Phys. Rev. Lett. **64**, 1824 (1990).

[17]T. Domański, A. Donabidowicz, K. I. Wysokiński, "Meservey-Tedrow-Fulde effect in a quantum dot embedded between metallic and superconducting electrodes", Phys. Rev. B **78**, 144515 (2008).

[18]R. Drost et al., "Combining electron spin resonance spectroscopy with scanning tunneling microscopy at high magnetic fields", Rev. Sci. Instrum. **93**, 043705 (2022).

[19]M. Eltschka et al., "Probing Absolute Spin Polarization at the Nanoscale", Nano Letters **14**, 7171 (2014).

[20]G. Falci, V. Bubanja, G. Schön, "Quasiparticle and Cooper pair tunneling in small capacitance Josephson junctions", Zeitschrift für Physik B Condensed Matter **85**, 451 (1991).

[21]E. Fernandes et al., "Adsorption sites of individual metal atoms on ultrathin MgO(100) films", Phys. Rev. B **96**, 045419 (2017).

[22]A. Ferrón et al., "Single spin resonance driven by electric modulation of the g-factor anisotropy", Phys. Rev. Research **1**, 033185 (2019).

[23]A. Floris et al., "Two-band superconductivity in Pb from ab initio calculations", Phys. Rev. B **75**, 054508 (2007).

[24]P. R. Forrester et al., "Antiferromagnetic MnNi tips for spin-polarized scanning probe microscopy", Rev. Sci. Instrum. **89**, 123706 (2018).

[25]R. Froidevaux, "Time-Resolved STM Measurements On Organic Molecules", Master thesis (EPFL, 2014).

[26]A. A. Golubov, M. Y. Kupriyanov, E. Il'ichev, "The current-phase relation in Josephson junctions", Rev. Mod. Phys. **76**, 411 (2004).

[27]S. A. González et al., "Photon-assisted resonant Andreev reflections: Yu-Shiba-Rusinov and Majorana states", Phys. Rev. B **102**, 045413 (2020).

[28]M. Graham, D. K. Morr, "Imaging the spatial form of a superconducting order parameter via Josephson scanning tunneling spectroscopy", Phys. Rev. B **96**, 184501 (2017).

[29]C. Grosse et al., "Quantitative mapping of fast voltage pulses in tunnel junctions by plasmonic luminescence", Appl. Phys. Lett. **103**, 183108 (2013).

[30]N. J. Harmon, M. E. Flatté, "Theory of spin-coherent electrical transport through a defect spin state in a metal/insulator/ferromagnet tunnel junction undergoing ferromagnetic resonance", Phys. Rev. B **98**, 035412 (2018).

[31] A. J. Heinrich et al., "Single-Atom Spin-Flip Spectroscopy", Science **306**, 466 (2004).

[32] B. W. Heinrich et al., "Protection of excited spin states by a superconducting energy gap", Nature Phys. **9**, 765 (2013).

[33] F. Herman, R. Hlubina, "Microscopic interpretation of the Dynes formula for the tunneling density of states", Phys. Rev. B **94**, 144508 (2016).

[34] F. Herman, R. Hlubina, "Thermodynamic properties of Dynes superconductors", Phys. Rev. B **97**, 014517 (2018).

[35] M. Hervé, M. Peter, W. Wulfhekel, "High frequency transmission to a junction of a scanning tunneling microscope", Appl. Phys. Lett. **107**, 093101 (2015).

[36] C. F. Hirjibehedin, C. P. Lutz, A. J. Heinrich, "Spin Coupling in Engineered Atomic Structures", Science **312**, 1021 (2006).

[37] J. Ibañez-Azpiroz et al., "Spin-fluctuation and spin-relaxation effects of single adatoms from first principles", Journal of Physics: Condensed Matter **30**, 343002 (2018).

[38] G.-L. Ingold, Y. V. Nazarov, "Charge Tunneling Rates in Ultrasmall Junctions", Single Charge Tunneling, Ch. 2, NATO ASI Series B, Vol. 294 (Plenum Press, New York, 1992), p. 22.

[39] G.-L. Ingold, H. Grabert, U. Eberhardt, "Cooper-pair current through ultrasmall Josephson junctions", Phys. Rev. B **50**, 395 (1994).

[40] B. Jäck et al., "Critical Josephson current in the dynamical Coulomb blockade regime", Phys. Rev. B **93**, 020504 (2016).

[41] P. Joyez, "Self-Consistent Dynamics of a Josephson Junction in the Presence of an Arbitrary Environment", Phys. Rev. Lett. **110**, 217003 (2013).

[42] P. Kot et al., "Microwave-assisted tunneling and interference effects in superconducting junctions under fast driving signals", Phys. Rev. B **101**, 134507 (2020).

[43] J. L. Lado, A. Ferrón, J. Fernández-Rossier, "Exchange mechanism for electron paramagnetic resonance of individual adatoms", Phys. Rev. B **96**, 205420 (2017).

[44] N. Lorente, J.-P. Gauyacq, "Efficient Spin Transitions in Inelastic Electron Tunneling Spectroscopy", Phys. Rev. Lett. **103**, 176601 (2009).

[45] S. Loth et al., "Controlling the state of quantum spins with electric currents", Nature Physics **6**, 340 (2010).

[46] S. Loth et al., "Measurement of Fast Electron Spin Relaxation Times with Atomic Resolution", Science **329**, 1628 (2010).

[47] S. Loth et al., "Bistability in Atomic-Scale Antiferromagnets", Science **335**, 196 (2012).

[48]G. I. Lykken et al., "Measurement of the Superconducting Energy Gap and Fermi Velocity in Single-Crystal Lead Films by Electron Tunneling", Phys. Rev. B **4**, 1523 (1971).

[49]L. Malavolti et al., "Tunable Spin–Superconductor Coupling of Spin 1/2 Vanadyl Phthalocyanine Molecules", Nano Lett. **18**, 7955 (2018).

[50]W. C. Martin, "Table of Spin-Orbit Energies for p-Electrons in Neutral Atomic (core) np Configurations", J Res Natl Inst Stan **75A**, 109 (1971).

[51]W. L. McMillan, "Tunneling Model of the Superconducting Proximity Effect", Phys. Rev. **175**, 537 (1968).

[52]J. Merkt, "Entwurf und Untersuchung einer Antenne für 84 GHz zur Strahlungseinkopplung in ein STM", Bachelor thesis (KIT, 2016).

[53]R. Meservey, P. M. Tedrow, P. Fulde, "Magnetic Field Splitting of the Quasiparticle States in Superconducting Aluminum Films", Phys. Rev. Lett. **25**, 1270 (1970).

[54]S. Nadj-Perge et al., "Observation of Majorana fermions in ferromagnetic atomic chains on a superconductor", Science **346**, 602 (2014).

[55]F. D. Natterer et al., "Reading and writing single-atom magnets", Nature **543**, 226 (2017).

[56]A. F. Otte et al., "Spin Excitations of a Kondo-Screened Atom Coupled to a Second Magnetic Atom", Phys. Rev. Lett. **103**, 107203 (2009).

[57]W. Paul et al., "Generation of constant-amplitude radio-frequency sweeps at a tunnel junction for spin resonance STM", Rev. Sci. Instrum. **87**, 074703 (2016).

[58]W. Paul et al., "Control of the millisecond spin lifetime of an electrically probed atom", Nat. Phys. **13**, 403 (2017).

[59]A. Pavlovska, E. Bauer, "A New Surface Reconstruction: Pb(110)", EPL **9**, 797 (1989).

[60]A. Pavlovska et al., "Preparation of clean smooth Pb and In surfaces in situ in UHV-SEM", Appl. Surf. Sci. **143**, 245 (1999).

[61]O. Peters et al., "Resonant Andreev reflections probed by photon-assisted tunnelling at the atomic scale", Nature Physics **16**, 1222 (2020).

[62]M. T. Randeria et al., "Scanning Josephson spectroscopy on the atomic scale", Phys. Rev. B **93**, 161115 (2016).

[63]J. Reina Gálvez et al., "Cotunneling mechanism for all-electrical electron spin resonance of single adsorbed atoms", Phys. Rev. B **100**, 035411 (2019).

[64]G. I. Rochlin, "Determination of the Anisotropy of the Energy Gap in Superconducting Pb by Superconductive Tunneling", Phys. Rev. **153**, 513 (1967).

[65] A. Roychowdhury et al., "Microwave Photon-Assisted Incoherent Cooper-Pair Tunneling in a Josephson STM", Phys. Rev. Applied **4**, 034011 (2015).

[66] M. Ruby et al., "Experimental Demonstration of a Two-Band Superconducting State for Lead Using Scanning Tunneling Spectroscopy", Phys. Rev. Lett. **114**, 157001 (2015).

[67] A. Savitzky, M. J. E. Golay, "Smoothing and Differentiation of Data by Simplified Least Squares Procedures", Analytical Chemistry **36**, 1627–1639 (1964).

[68] E. Scheer et al., "The signature of chemical valence in the electrical conduction through a single-atom contact", Nature **394**, 154 (1998).

[69] S. Schintke et al., "Insulator at the Ultrathin Limit: MgO on Ag(001)", Phys. Rev. Lett. **87**, 276801 (2001).

[70] T. S. Seifert et al., "Single-atom electron paramagnetic resonance in a scanning tunneling microscope driven by a radio-frequency antenna at 4 K", Phys. Rev. Research **2**, 013032 (2020).

[71] J. Senkpiel et al., "Single channel Josephson effect in a high transmission atomic contact", Communications Physics **3**, 131 (2020).

[72] E. Snider et al., "Room-temperature superconductivity in a carbonaceous sulfur hydride", Nature **586**, 373 (2020).

[73] M. Steinbrecher et al., "Quantifying the interplay between fine structure and geometry of an individual molecule on a surface", Phys. Rev. B **103**, 155405 (2021).

[74] P. M. Tedrow, R. Meservey, "Direct Observation of Spin-State Mixing in Superconductors", Phys. Rev. Lett. **27**, 919 (1971).

[75] P. K. Tien, J. P. Gordon, "Multiphoton Process Observed in the Interaction of Microwave Fields with the Tunneling between Superconductor Films", Phys. Rev. **129**, 647 (1963).

[76] M. Tinkham, "Introduction to Superconductivity" (Dover Publications, 2004).

[77] P. Townsend, J. Sutton, "Investigation by Electron Tunneling of the Superconducting Energy Gaps in Nb, Ta, Sn, and Pb", Phys. Rev. **128**, 591 (1962).

[78] M. Uhl et al., "Multiband Josephson Effect in a Pb Tunnel Junction", in preparation (2023).

[79] B. V. Vasiliev, "The critical temperature of superconductor and its electronic specific heat", arXiv:1008.1446v1 (2010).

[80] L. M. Veldman et al., "Free coherent evolution of a coupled atomic spin system initialized by electron scattering", arXiv:2101.10765 (2021).

[81] S. Westerdale, "Superconducting Metals: Finding Critical Temperatures and Observing Phenomena" (MIT Department of Physics, 2010).

⁸²P. Willke et al., "Hyperfine interaction of individual atoms on a surface", Science **362**, 336 (2018).

⁸³P. Willke et al., "Probing quantum coherence in single-atom electron spin resonance", Sci. Adv. **4**, eaaq1543 (2018).

⁸⁴P. Willke et al., "Magnetic resonance imaging of single atoms on a surface", Nat. Phys. **15**, 1005 (2019).

⁸⁵H.-N. Yang et al., "Observation of a Novel Double-Step Phase in Pb(110) Surface", EPL **19**, 215 (1992).

⁸⁶K. Yang et al., "Engineering the Eigenstates of Coupled Spin-1/2 Atoms on a Surface", Phys. Rev. Lett. **119**, 227206 (2017).

⁸⁷K. Yang et al., "Electrically controlled nuclear polarization of individual atoms", Nature Nanotech. **13**, 1120 (2018).

⁸⁸K. Yang et al., "Coherent spin manipulation of individual atoms on a surface", Science **366**, 509 (2019).

10 Curriculum Vitae

Personal Details

Name	Maximilian Uhl
Date of Birth	April 21, 1993
Place of Birth	Augsburg, Germany
Nationality	German

Education

10/2011 - 09/2014	Bachelor of Science in Physics at Augsburg University, Minor Subject: Informatics, Bachelor Thesis: Elektronengitter-diskretisierung in zweidimensionalen hexagonalen Flachbandsystemen (Electron Lattice Discretization in Two-Dimensional Hexagonal Flat Band Systems)
10/2014 - 05/2017	Master of Science in Physics at Augsburg University, Minor Subject: Mathematics, Master Thesis: Quantum Dynamics in Graphene with Arbitrary Time- and Space-Dependent Potential Barriers
04/2017 - 03/2023	PhD in Experimental Physics at Max Planck Institute for Solid State Research / Stuttgart University, PhD Thesis: Scanning Tunneling Microscopy of Superconductors and High Field Electron Spin Resonance

11 Selbständigkeitserklärung (deutsch)

Schriftliche Bestätigung der eigenständig erbrachten Leistung gemäß § 6 Absatz 3 der Promotionsordnung von 2016 der Universität Stuttgart

Die eingereichte Dissertation zum Thema

Scanning Tunneling Microscopy of Superconductors
and High Field Electron Spin Resonance

stellt meine eigenständig erbrachte Leistung dar.

Ich habe ausschließlich die angegebenen Quellen und Hilfsmittel benutzt. Wörtlich oder inhaltlich aus anderen Werken übernommene Angaben habe ich als solche kenntlich gemacht.

Die Richtigkeit der hier getätigten Angaben bestätige ich und versichere, nach bestem Wissen die Wahrheit erklärt zu haben.

Stuttgart, den